

Retrieval of cloud fraction and optical thickness of liquid water clouds over ocean from multi-angle polarization observations

Claudia Emde^{1,2}, Veronika Pörtge¹, Mihail Manev¹, and Bernhard Mayer¹

¹Meteorologisches Institut, Ludwig-Maximilians-Universität München, Germany

²Institut für Physik der Atmosphäre, Deutsches Zentrum für Luft- und Raumfahrt (DLR), Germany

Correspondence: Claudia Emde (claudia.emde@lmu.de)

Abstract. ~~We introduce an innovative~~

~~We introduce a novel~~ method to retrieve ~~the~~ cloud fraction and ~~optical thickness based on the degree of polarization at two scattering angles~~ the optical thickness of liquid clouds over a water surface based on polarimetry. The approach is well-suited for satellite observations providing multi-angle polarization measurements, ~~such as in particular~~ the Hyper-Angular Rainbow Polarimeter #2 (HARP2), ~~the Spectro-Polarimeter for Planetary EXploration (SPEX), and the Multi-viewing Multi-channel Multi-polarisation Imager (3MI). The cloud fraction can be derived independently of~~. Unlike commonly used methods to derive the cloud fraction our method does not depend on the spatial resolution of the observations, and it does not require any threshold values for cloud detection. Based on radiative transfer simulations we show that the cloud fraction and the cloud optical thickness for each pixel can be derived from measurements at two scattering-viewing angles: one within cloudbow at a scattering angle of approximately 40° the cloudbow and a second, preferably around 90° in the sun-glint region. In the cloudbow, the degree of polarization depends mainly on the cloud optical thickness and not on the cloud cover, as only cloud scattering produces significant polarization. Conversely, at scattering angles around 90°, water surface reflection and molecular scattering produce polarization, making for a viewing direction in the sun-glint region, the degree of polarization dependent depends on the clear fraction of the pixel. Using, because here the radiation scattered by cloud droplets is almost unpolarized whereas radiation reflected by the surface is highly polarized. Utilizing these dependencies, we developed a straightforward retrieval algorithm using a retrieval using a simple lookup-table approach, easily implemented with a one-dimensional vector radiative transfer code. Based on sensitivity studies, we show that prior information about wind speed and aerosol optical thickness improves the accuracy of the cloud fraction retrieval. Prior information about the cloud droplet size distribution can reduce the uncertainty of the cloud optical thickness retrieval. The prior information should be obtained by combining our method with already existing retrieval algorithms. We also investigated 3D scattering effects and found that the cloud optical thickness is generally underestimated due to neglecting 3D scattering effects. The cloud fraction is overestimated in cloud shadows and underestimated in the in-scattering regions.

As a demonstration, we apply the methodology ~~on air-borne to airborne~~ observations from polarization cameras of the Munich Aerosol Cloud Scanner (specMACS) instrument. The high spatial resolution data (10-20 m) has been averaged to a spatial resolution of approximately 2.5 km to mimic satellite observations. ~~Comparison of the derived cloud fractions with the high spatial resolution images for specific cases, featuring~~ From the average linear polarization at scattering angles of 140°

and 110° we derive continuous cloud fraction values and the corresponding cloud optical thicknesses. The comparison for cases including low, medium, and high cloud fractions, demonstrates the expected performance of the retrieval. shows that the retrieval, using only the reflected polarized radiances at two scattering angles, provides accurate estimates of the cloud fraction for observations with coarse spatial resolution.

Copyright statement. TEXT

1 Introduction

Clouds influence local weather conditions as well as the Earth's climate system. They affect the energy balance and play a large role in the planet's long-term climate. According to the latest IPCC assessment report AR6 (Intergovernmental Panel On Climate Change, 2023), there have been major advances in the understanding of cloud processes over the last decade that have decreased the uncertainty range for the cloud feedback by about 50% compared to AR5 (Intergovernmental Panel On Climate Change, 2014) but nevertheless, clouds remain the largest contribution to the overall uncertainty in climate feedbacks.

In order to further improve the representation of clouds in climate models more observations are required. Important quantities to characterize the interaction of radiation with cloud droplets or particles are the cloud phase, the cloud optical thickness, the cloud fraction and the droplet or particle size distribution.

A commonly used method to derive the cloud optical thickness and effective droplet size for model validation. The Cloud Assessment Group of the GEWEX (Global Energy and Water Exchanges) program gathers cloud products derived from active and passive satellite observations in the solar spectral region is based observations at two wavelengths, a non-absorbing one in the visible which is sensitive only to cloud optical thickness, and an absorbing one in the near-infrared which also depends on the droplet size (Nakajima and King, 1990). This methodology is included in operational retrieval algorithms (e.g. for the Moderate Resolution Imaging Spectroradiometer MODIS, Platnick et al., 2017).

MODIS and thermal spectral regions (Stubenrauch et al., 2024) and provides a database of publicly available, global cloud products at a spatial resolution of 1° latitude \times 1° longitude. They also provide recommendations on how satellite-retrieved cloud properties may be used in climate studies and climate model evaluation. One important parameter is the global cloud fraction, for which they obtain an average of 0.66 ± 0.04 from eleven participating datasets. The standard method to derive cloud fraction from space is to calculate the fraction of image pixels that contain some clouds. E.g., for MODIS, which has a relatively high spatial resolution of about $1 \times 1 \text{ km}^2$. Among the MODIS cloud products is also, the cloud fraction which is retrieved on a spatial resolution of $5 \times 5 \text{ km}^2$ by computing the ratio of pixels where clouds have been detected and the clear pixels for this larger region including 25 individual MODIS pixels.

An alternative approach to retrieve droplet size and also information on the droplet size distribution is based on polarimetric observations of (Platnick et al., 2017). The determination of cloud fraction from satellite measurements is problematic for various reasons: First, there is no quantitative cloud definition, e.g. a lower liquid water content limit. Secondly, most cloud

detection methods rely on thresholds, which depend on instrument and algorithm performance as well as on cloud assumptions and on the cloudbow. This method has been first applied to derive the microphysical properties of the sulfuric acid clouds on Venus (Hansen and Hovenier, 1974). For Earth, it has been used to derive liquid water cloud droplet size distributions from satellite observations using the POLarization and Directionality of the Earth's Reflectances (POLDER) instrument (Bréon and Doutriaux-Bonville, 2002) and to air-borne observations with high spatial resolution (Alexandrov et al., 2012; Pörtge et al., 2023). Similarly as for Venus, average liquid cloud properties have been retrieved for Earth via Earthshine observations (Sterzik et al., 2020).
Thirdly, the definition of cloud fraction based on the fraction of cloudy pixels in an image depends on the viewing direction and strongly on the spatial resolution of the observations (e.g. Wielicki and Parker, 1992).

Di Girolamo and Davies (1997) developed a pattern recognition approach to correct for the spatial distribution error. Dutta et al. (2020) applied this method to correct for the spatial resolution error in Multi-angle Imaging SpectroRadiometer (MISR) observations and found cloud fraction reductions of more than 0.4 in regions dominated by shallow cumulus clouds. They validated the resolution-corrected cloud product by comparison to Advanced Spaceborne Thermal Emission and Reflection Radiometer (ASTER) observations of 15 m resolution and show that the 50°N to 50°S cloud fraction, which is in accordance to the GEWEX assessment of about 0.65 in the uncorrected MISR cloud product, is reduced to 0.47 in the resolution corrected cloud product.

The An alternative resolution-independent cloud fraction retrieval approach is implemented in the aerosol retrieval algorithm based on an optimal estimation approach developed by (Hasekamp, 2010) derives apart from optimal estimation by Hasekamp (2010), which provides, in addition to aerosol optical properties also, the cloud fraction from POLDER measurements with a spatial resolution of about $7 \times 6 \text{ km}^2$. In a validation study for partially cloudy scenes based on simulated data, the retrieval has been validated by (Stap et al., 2016a, b) and it has been shown Stap et al. (2016a, b) show that the retrieved cloud fraction correlates well with the cloud fraction used as input for radiative transfer simulations to produce the simulated data. Similarly, Van Diedenhoven et al. (2007) developed a retrieval method for cloud parameters from satellite-based reflectance measurements (Global Ozone Monitoring Experiment (GOME) and Scanning Imaging Absorption Spectrometer for Atmospheric Chartography (SCIAMACHY)) in the ultraviolet and the oxygen A-band. Based on an optimal estimation approach they derive cloud fraction, cloud optical thickness, and cloud top pressure. The oxygen A-band contains information about cloud optical thickness and cloud top pressure. The UV spectral region is also sensitive to cloud fraction, because the larger the clear part since the Rayleigh scattering contribution to the reflectance increases with the clear fraction of the pixel the higher the Rayleigh scattering contribution to the reflectance. Note that these algorithms do not rely on thresholds for cloud detection because the cloud fraction is not defined by a fraction of cloudy pixel but solely derived from the observed reflected radiation and it is therefore a resolution-independent continuous quantity.

In this study, we propose a similar method to estimate the cloud fraction of liquid water clouds over ocean. It makes use of the angular dependence of the degree of linear polarization of reflected radiation. For clouds, it becomes large in the cloudbow region, whereas for clear sky above ocean, it becomes large in the sun-glint region. Therefore, we propose to measure the degree of linear polarization at two angles, one in the cloudbow region to retrieve the vertical cloud optical thickness of the cloudy part and another angle in the sun-glint region to retrieve cloud fraction.

~~In the near future new satellite missions including polarimetry are scheduled. Next (launch in February 2024) is the~~ The global cloud cover cannot be obtained using our method because it is developed only for liquid clouds over ocean. Since ice
95 clouds do not produce a cloudbow, the methodology cannot directly be applied to determine the cloud fraction and the optical thickness of ice clouds. However, it would be possible to replace the degree of linear polarization in the cloudbow region by an intensity observation at the same angle to retrieve the ice cloud optical thickness. For retrievals over land, polarization due to surface reflection is too small to be used for a cloud fraction retrieval. Therefore an additional method needs to be developed which could use the strong polarization caused by Rayleigh scattering between the clouds to obtain information about the
100 cloud fraction. This method should use shorter wavelengths which are mostly insensitive to surface properties and for which the Rayleigh scattering contribution is much higher.

The resolution-independent cloud fraction retrieval method could be a valuable addition to operational cloud retrieval algorithms for upcoming satellite instruments providing multi-angle polarization observations. The NASA Plankton, Aerosol, Cloud, ocean Ecosystem (PACE) mission (<https://pace.oceansciences.org>) which ~~will include~~ has successfully been launched
105 on 8th of February 2024 includes two polarimeters, the Spectro-polarimeter for Planetary Exploration (SPEXone) and the ~~Hyper-Angular Research Polarimeter~~ Hyper-Angular Research Polarimeter #2 (HARP2). ~~SPEXone will provide~~ (Remer et al., 2019)
. SPEXone provides hyper-spectral polarized radiances in the spectral range from 385–770 nm in five viewing directions for a narrow swath of 100 km at nadir. The spatial resolution is about ~~2.55~~ 2.55 km and global coverage is obtained after approximately 30 days. HARP2 is a hyper-angular instrument ~~and includes~~, with four spectral bands between 440 nm and 870 nm and ~~will~~
110 ~~observe~~ observes a wide swath of 1555 km at nadir. For ~~670~~ the 669 nm band HARP2 includes 60 viewing angles spaced over 114°. The spatial resolution is ~~with about 3 slightly less than SPEXone. Due to the wider swath global coverage can be obtained in two days.~~

approximately the same as SPEXone. The Multi-Viewing Multi-Channel Multi-Polarisation Imaging (3MI) instrument is an optical radiometer dedicated ~~primarily to aerosol characterization (Fougnie et al., 2018, <https://www.eumetsat.int/eps-sg-3mi>)~~
115 to aerosol and cloud characterization (Fougnie et al., 2018). It is one of the missions of the EUMETSAT Polar System Second Generation (EPS-SG) program planned to be launched in 2025. It will provide a multi-spectral (from 410 to 2130 nm), multi-polarisation (-60° , 0° , and $+60^\circ$), and multi-angular (14 views) image of the ~~Earth~~ Earth-outgoing radiance at the top of the atmosphere. The spatial resolution is 4 km at nadir and the swath width is ~~2200×2200~~. ~~A secondary mission objective is to improve the cloud characterisation, in particular cloud phase, cloud microphysics (phase and effective particle size) cloud~~
120 ~~height, and cloud optical depth~~ km.

Since cloud structures change rapidly, observations at the two suggested scattering angles should ideally be taken nearly simultaneously. HARP2 is designed to provide such observations, so it is ideally suited for our proposed method. For SPEXone and 3MI, further investigations on the collocation of the observations would be required.

~~In this paper we present a novel method to retrieve the cloud optical thickness along with the cloud fraction, which could~~
125 ~~be a valuable addition to operational cloud retrieval algorithms for up-coming satellite instruments providing multi-angle polarization observations. The retrieval method requires the degree of linear polarization at two angles, one in the cloudbow region sensitive mainly to cloud optical thickness and another angle, preferably at a scattering angle around 90° which is~~

mainly sensitive to the cloud fraction. Such observations will be available from HARPS, SPEXone and 3MI. Our method performs best over ocean, because of the high polarization of the sun glint, which causes a clear correlation between degree of polarization and the cloud fraction.

The paper is structured as follows: In Section 2 the [setup of the radiative transfer model for 1D and 3D simulations is described. In Section 3, the](#) dependence of the degree of polarization on cloud optical thickness and cloud fraction is investigated and retrieval lookup tables for different atmosphere and surface conditions are constructed ~~to show how~~. [In Section 4, 3D scattering effects on the](#) cloud fraction and cloud optical thickness ~~can be retrieved independently~~ [retrieval are investigated.](#)
In Section 5, we apply the retrieval method ~~on to~~ airborne observations of the specMACS instrument ~~and present the results.~~
The final Section 6 includes a [brief](#) summary, discusses limitations and provides an outlook on future work.

2 Methodology

2.1 General setup

For all simulations we used the ~~Monte Carlo~~ radiative transfer model MYSTIC ([Mayer, 2009; Emde et al., 2010](#)) ~~(Monte carlo code for the~~ implemented in the libRadtran package (Mayer and Kylling, 2005; Emde et al., 2016). MYSTIC is a comprehensive polarized vector radiative transfer model that can be run in 1D or 3D, plane-parallel or spherical geometry. ~~For this study we applied the freely available 1D plane-parallel version that~~ It has been extensively validated in various model intercomparison studies, e.g. [Emde et al. \(2015\)](#) ~~(e.g., Emde et al., 2015, 2018).~~

The general setup for all simulations is as follows: we take the US-standard atmosphere from Anderson et al. (1986) to ~~setup the model layers~~ [set up the profiles of pressure, temperature, and trace gas concentrations.](#) As incoming solar irradiance we ~~include the simulated~~ [use the extraterrestrial](#) spectrum by Kurucz and Bell (1995). We enable the polarisation mode (Emde et al., 2010) to compute the complete Stokes vector, and the variance reduction methods (Buras and Mayer, 2011) for accurate simulations including cloud scattering. We perform monochromatic simulations at ~~669~~667 nm, [approximately](#) the center wavelength of the ~~HARPS instrument~~ [HARP2 instrument where 60 scattering angles are observed simultaneously.](#) The solar zenith angle is set ~~to~~ 50°. ~~Simulations~~ [The simulations](#) are performed for viewing angles from -60° to +60° in steps of 1° in the solar principal plane, thus we obtain the Stokes vector for scattering angles Θ from ~~-110~~70° to ~~110~~180°. The scattering angle is defined as the angle between the sun position vector ([incident direction](#)) and viewing direction vector (i.e., ~~at 0°~~ the sun is behind the observer) ~~at 180°~~. [As we will show later \(see Fig. 4 \(g\)\), the retrieval performs best for observations in the solar principal plane including the maximum of the sun glint.](#)

~~All simulations are performed for a clear sky atmosphere and for a cloud layer located from 2–3, respectively. The optical thickness of the cloud is varied between 1 and 50. Cloud droplet sizes are gamma distributed with an effective radius of 10 and an effective variance of 0.1. Cloud optical properties were calculated using the Mie program included in libRadtran (Mie, 1908; Wiscombe, 1980).~~

The components of Stokes vector \mathbf{I} are ~~definind~~defined as time averages of linear combinations of the electromagnetic field vector (~~Chandrasekhar, 1950; Hansen and Travis, 1974~~)(e.g., Chandrasekhar, 1950; Hansen and Travis, 1974):

$$I = \langle E_{\parallel} E_{\parallel}^* + E_{\perp} E_{\perp}^* \rangle, \quad (1)$$

$$Q = \langle E_{\parallel} E_{\parallel}^* - E_{\perp} E_{\perp}^* \rangle, \quad (2)$$

$$U = \langle E_{\parallel} E_{\perp}^* + E_{\perp} E_{\parallel}^* \rangle, \quad (3)$$

$$V = i \langle E_{\parallel} E_{\perp}^* - E_{\perp} E_{\parallel}^* \rangle. \quad (4)$$

Here, E_{\parallel} and E_{\perp} are the components of the electric field vector parallel and perpendicular to the reference plane, respectively. I is the intensity of the radiation, Q and U give the state of linear polarization and V the circular polarization. The unit of the Stokes components is $\text{W}/(\text{m}^2 \text{ nm sr})$. We will neglect V in the following because circular polarization is several orders of magnitude smaller than linear polarization (e.g., Emde et al., 2018). In the solar principal plane, U is exactly 0 for plane-parallel geometry by definition. Therefore the signed degree of linear polarization is given by

$$P = Q/I \quad (5)$$

A negative (positive) P means that the radiation is predominantly polarized perpendicular (parallel) to the scattering plane. Note that P is a dimensionless quantity which can be measured without absolute calibration. For 3D geometry, U can be non-zero and we use the following equation to calculate the signed degree of linear polarization:

$$P = - \frac{\sqrt{Q^2 + U^2}}{I} \quad (6)$$

The negative sign indicates that the radiation is predominantly polarized in the direction perpendicular to the scattering plane, i.e. P has the same sign as Q/I in the solar principal plane.

In the following, we call the directional dependence of radiance on the scattering angle $\mathbf{I}(\Theta)$ the “phase curve” and the directional dependence of the degree of polarization $P(\Theta)$ the “polarimetric polarized phase curve”.

2.1 Retrieval of cloud optical thickness and cloud cover from degree of polarization

~~In this section we analyse the sensitivity of the polarimetric phase curve on cloud fraction and cloud optical thickness. Further we investigate the impact of wind speed, aerosols and cloud altitude.~~

2.0.1 Sensitivity and retrieval lookup tables for ocean surface

~~Left: Sensitivity of phase curve on cloud optical thickness τ at 667 nm. Right: Phase curve for fixed $\tau = 5$ for various cloud fractions. All simulations are for an ocean surface, a wind speed of 5 m/s and a solar zenith angle of 50°. Cloud droplets sizes are modeled using a gamma distribution with an effective radius of 10 nm and an effective variance of 0.1. In the following we include an ocean surface which is modelled~~ The polarized bidirectional reflectance distribution matrix of the ocean surface

is modeled using the reflectance matrix based on the Fresnel equations convolved with a Gaussian kernel to account for the ocean waves (Mishchenko and Travis, 1997; Tsang et al., 1985; Cox and Munk, 1954a, b). Water surface reflection causes very strong polarization in the sun-glint. The wind speed which determines the spread of the sun-glint region is set to 5 m/s if not specified otherwise. In this study, land surfaces are assumed to be Lambertian reflectors, i.e. reflected radiation is completely unpolarized.

2.1 Model setup for 1D radiative transfer simulations and independent pixel approximation

All 1D simulations are performed for a clear sky atmosphere and for a liquid cloud layer located from 2–3 km, respectively. The optical thickness of the cloud is varied between 1 and 50. Cloud droplet sizes are gamma distributed with an effective radius of 10 μm and an effective variance of 0.1. Cloud optical properties were calculated using the Mie program included in libRadtran (Mie, 1908; Wiscombe, 1980). Note that this simple setup is only used to illustrate the main sensitivities to cloud fraction and cloud optical thickness. Sensitivity studies with different model parameters are performed later in Sections 3.2 and 3.3.

In order to calculate the Stokes vector for a partially cloudy pixel we combine the clear and the cloudy simulations, which is commonly called independent pixel approximation (IPA):

$$\mathbf{I} = (1 - c) \cdot \mathbf{I}_{\text{clear}} + c \cdot \mathbf{I}_{\text{cloudy}} \quad (7)$$

Here c is the cloud fraction of the pixel, $\mathbf{I}_{\text{clear}}$ is the Stokes vector simulated for clear sky, and $\mathbf{I}_{\text{cloudy}}$ is the Stokes vector simulated for the cloudy sky. The degree of linear polarization of a partially cloudy pixel in the principal plane is

$$P = - \frac{(1 - c)Q_{\text{clear}} + cQ_{\text{cloudy}}}{(1 - c)I_{\text{clear}} + cI_{\text{cloudy}}} \quad (8)$$

Note that it cannot be calculated as the linear combination of the individual degrees of polarization.

2.2 Model setup for 3D radiative transfer simulations

2.2.1 2D cloud scene with sharp cloud edge

In order to quantify the impact of 3D cloud scattering systematically we define a scene, where half of the domain is cloud covered and the other half is clear sky. In this case, we can distinguish the two basic 3D effects: in-scattering, when the cloud side is illuminated, and shadowing, when the cloud casts a shadow on the surface. Such a sharp cloud edge is of course an extreme case for which we may expect the most significant 3D effects.

The 2D cloud is included in the same background atmosphere that is used for the 1D simulations (Section 2.1). The cloud height is between 1 and 2 km. As before the effective radius of the cloud droplets is set to 10 μm and the vertical optical thickness is varied between 1 and 50. The wind speed is set to 5 m/s and the simulations are performed without aerosols. The domain size was set to 100 km with the cloud edge in the center. We simulate polarized observations of the step cloud at the top of the atmosphere at a spatial resolution of 500 m in x -direction. Results of those simulations-

2.2.2 Randomly distributed box clouds

The second scenario should resemble shallow cumulus cloud fields with different cloud fractions. We define 5×5 pixels with a spatial resolution of $500 \times 500 \text{ m}^2$ and randomly fill the pixels with clouds, this way we get cloud fields with cloud fractions of $\{1/25, 2/25, \dots, 25/25\}$. The geometrical thickness of the clouds is 100 m, typical for shallow cumulus fields (e.g. Zhan et al., 2021). MYSTIC applies periodic boundary conditions, that means that the same clouds are repeated horizontally in x and y directions. The background atmosphere and cloud microphysical properties are the same as for the 2D cloud edge (Section 2.2.1). We include an ocean surface and as before the wind speed is set to 5 m/s. We sample polarized radiances at the top of the atmosphere at a spatial resolution of $500 \times 500 \text{ m}^2$.

3 Setup of the retrieval

In this section we analyze the sensitivity of the polarized phase curve on cloud fraction and cloud optical thickness based on 1D radiative transfer simulations and the IPA approximations. In addition, we investigate the impact of wind speed, aerosols, and cloud altitude.

3.1 Phase curves for broken liquid clouds above an ocean surface

Results of the 1D simulations including an ocean surface and a cloud layer as defined in Section 2.1 are shown in the left panel of Figure 1. The blue line corresponds to the clear sky simulation. The top panel shows the total intensity I , the middle panel the linearly polarized intensity which is equal to the Q -component of the Stokes vector in the solar principal plane, and the bottom panel is the degree of linear polarization Q/I . The U -component of the Stokes vector is zero in the principal plane. The figures clearly show the broad sun-glint region at scattering angles around -110 to 100° . The degree of linear polarization of the sun-glint is close to 1 for clear sky (see blue line in lower left panel). The Q -component (middle left panel) is negative which means that the polarization direction is perpendicular to the scattering plane.

The grey lines in the left panels correspond to various cloud optical thicknesses from 1 (dark grey) to 50 (light grey). The intensity (unpolarized radiance I) increases with increasing cloud optical thickness since more radiation is reflected. The linearly polarized radiance Q saturates relatively quickly around $\tau = 5$. All curves show two distinct features, the cloudbow at scattering angles around -40 to 140° and the backscatter glory around 0 to 180° . In particular the cloudbow is highly polarized.

Looking at the Q -results we find that the linear polarization predominantly emerges from surface reflection at scattering angles around -110 to 80° and mainly from cloud scattering at scattering angles around -40 to 140° .

We then calculate the Stokes vector for a fixed cloud optical thickness of 5 for various cloud fractions, which can be simulated by combining the clear and the cloudy simulations, this approach is commonly called independent pixel approximation (IPA):

$$\underline{\mathbf{I}} = (1 - c) \cdot \underline{\mathbf{I}}_{\text{clear}} + c \cdot \underline{\mathbf{I}}_{\text{cloudy}}$$

Results for cloud fractions between 1/8 and 1 (fully cloudy), the results are shown in the right panels of Fig. 1. The black line corresponds to full cloud cover ($c=1$) and is identical to the line for $\tau=5$ in the left panels. When we focus on the degree of linear

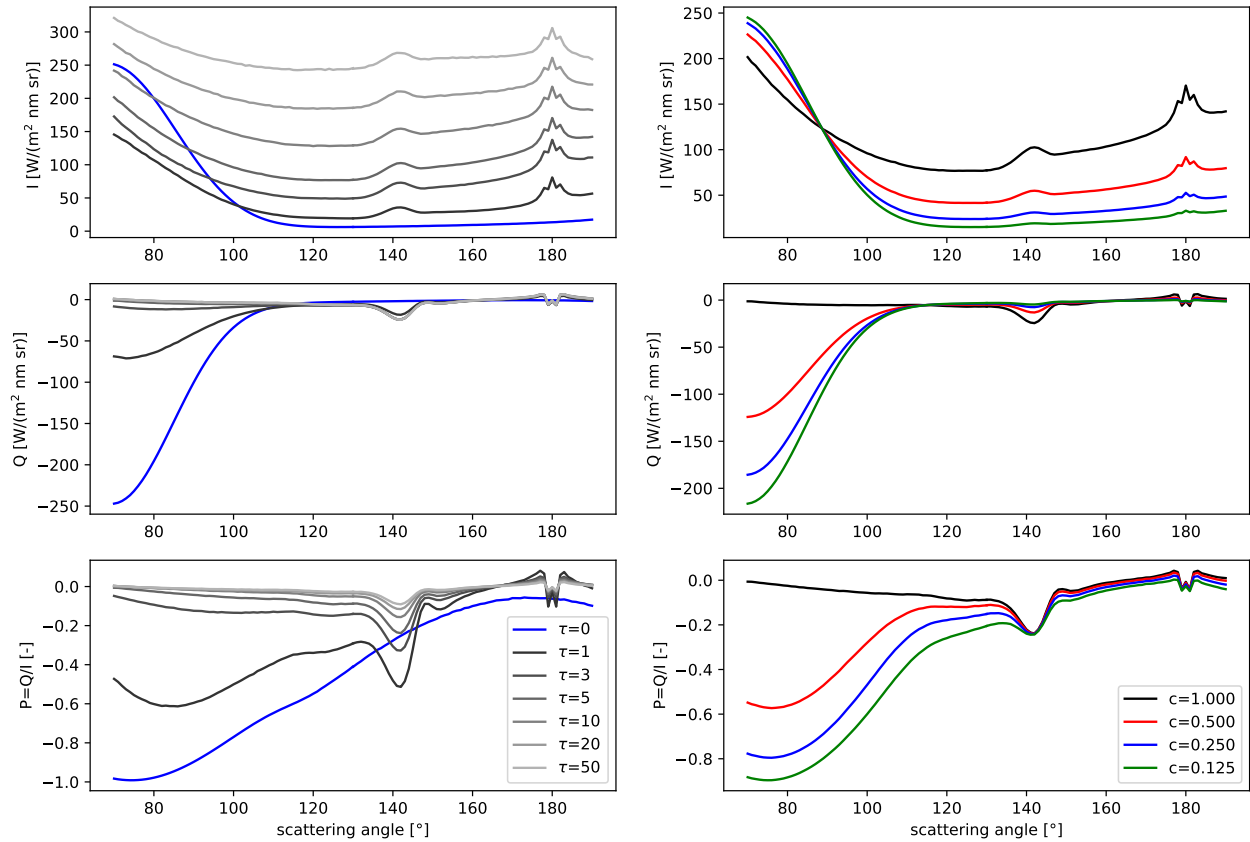


Figure 1. *Left:* Sensitivity of phase curve on cloud optical thickness τ at 667 nm. *Right:* Phase curve for fixed $\tau = 5$ for various cloud fractions. All simulations are for an ocean surface, a wind speed of 5 m/s and a solar zenith angle of 50° . Cloud droplets sizes are modeled using a gamma distribution with an effective radius of $10 \mu\text{m}$ and an effective variance of 0.1.

polarization Q/I we see ~~that~~ that it does not depend on cloud fraction in the cloudbow region, whereas there is a strong dependence on cloud fraction in the glint region. The reason is that surface reflection ~~only produces polarization in the glint region. When the pixel is partly cloudy causes strong polarization for angles smaller than about 110° . For partly cloudy pixels~~ a part of the surface is seen by the observer, ~~therefore and therefore~~ the degree of polarization is increased in glint directions compared to fully cloudy pixels. In the cloudbow region, only the cloud contributes to the degree of linear polarization, therefore the degree of linear polarization is not changed when a part of the surface becomes visible.

Using these dependencies allows us to generate a retrieval lookup table as illustrated in Figure 2. Here, we plotted the degree of polarization at $\Theta = 40^\circ$ ($P(40^\circ)$) on the x-axis and the degree of polarization at $\Theta = 90^\circ$ ($P(90^\circ)$) on the y-axis. The blue lines correspond to constant cloud fraction values, i.e. the upper light blue line is for a cloud fraction of 1.0 (fully cloudy) and the lower dark blue line is for a cloud fraction of 0.1. The grey lines correspond to constant cloud optical thickness values between 3 (dark grey) and 50 (light grey).

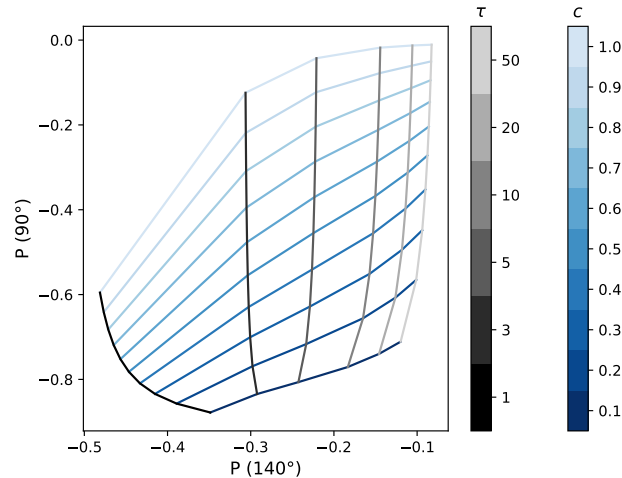


Figure 2. Lookup table for cloud cover and cloud optical thickness retrieval. The blue lines correspond to constant cloud fractions and the grey lines correspond to constant cloud optical thickness values.

The lookup-table plot illustrates, that cloud fraction and cloud optical thickness can be retrieved from the degree of linear polarization observed at the two scattering-viewing angles since the blue and green lines nicely separate grey lines separate nicely. Note that, since the cloud fraction is derived from the observation in the sun-glint, the retrieved cloud fraction corresponds to the cloud fraction of the pixel observing the glint.

3.1.1 Retrieval lookup tables for various scenarios

3.2 Retrieval lookup tables for various scenarios

Fig. 3 shows polarimetric-polarized phase curves and the corresponding lookup tables for various scenarios. The upper row (a) corresponds to the scenario presented in the previous section, with an ocean surface and a wind speed of 5 m/s.

In order to test the dependency of the polarimetric phase curve on the wind speed we performed the same simulations for To investigate the influence of wind speed on the polarized phase curve, we conducted identical simulations with a wind speed of 10 m/s (scenario (b)). We find that the maximum degree of polarization of $|P|$ for partially cloudy pixels is decreased and also the slope of P is smaller between -90° $|P|$ is smaller for scattering angles between 90° and -70° 110° scattering angle. The lookup table. The lookup table generated for higher wind speeds looks very similar and is also well suited similar to that of the previous case and is just as good to retrieve optical thickness and cloud fraction.

The presence of aerosols also modifies the polarization state. Therefore, we repeated the simulations with additional aerosols corresponding to the mixture “maritime clean” as defined in the OPAC database (Hess et al., 1998; Emde et al., 2016) with an aerosol optical thickness set to 0.1 (scenario (c)). Comparing Compared to the results without aerosols, we find that the degree of polarization is slightly decreased due to increased multiple scattering, as expected. Apart from that the polarimetric phase

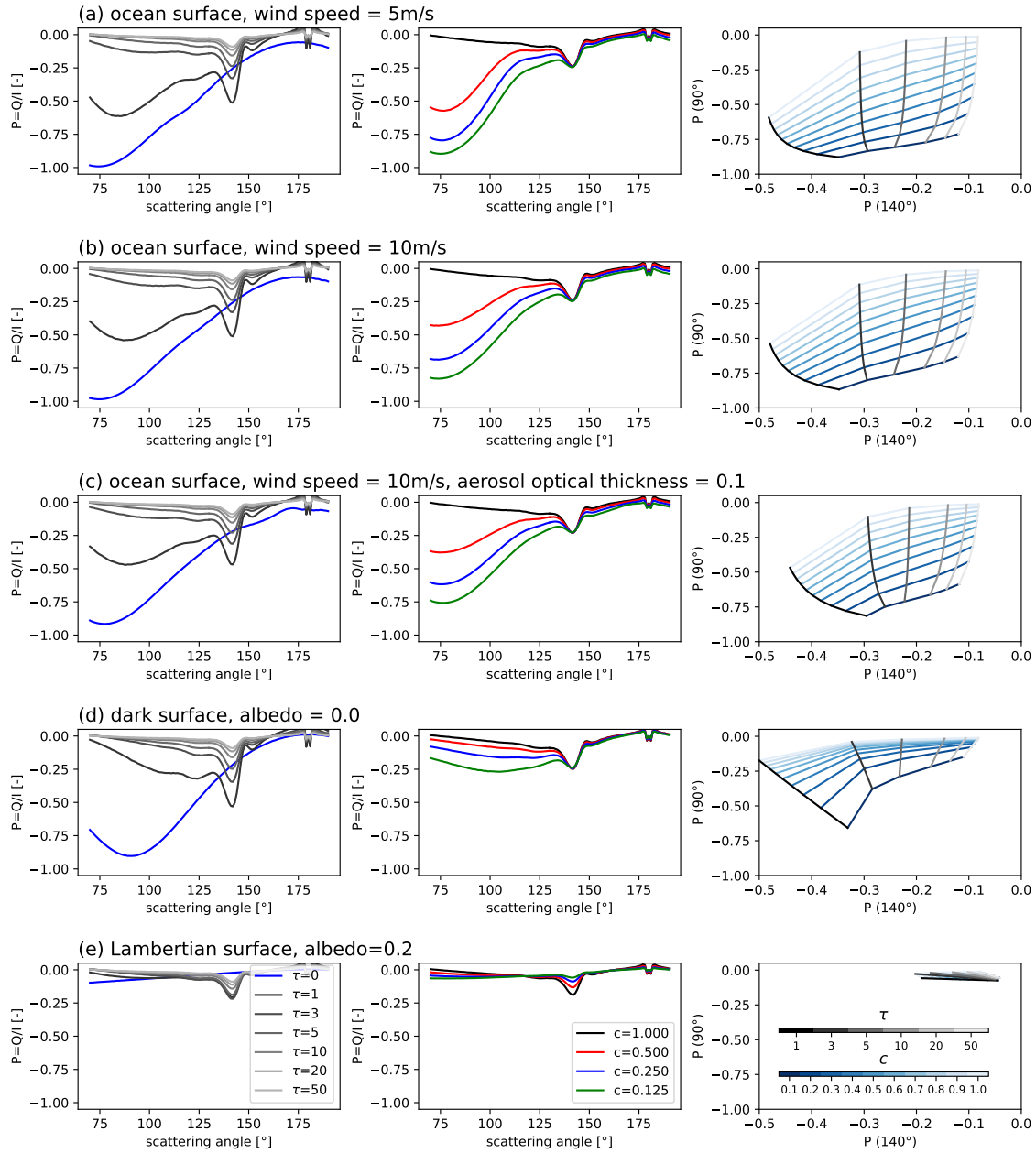


Figure 3. Polarimetric-Polarized phase curves and retrieval lookup tables for various scenarios. The left figures shows simulation show simulations for a homogeneous cloud layer and the grey lines correspond to different cloud optical thicknesses. The blue lines corresponds correspond to the clear-sky-clear-sky simulation. The middle plots show the polarimetric-polarized phase curves for partially cloudy pixels. The right panels shows show the corresponding retrieval lookup tables, the line colors correspond to Fig.2.

curves. Furthermore, the polarized phase curves closely follow the same pattern as the scenario (a) and also the lookup-table look very similar. lookup table appears nearly identical.

Finally, we may test whether the methodology would also work for land surfaces. We use as an approximation a Lambertian surface as an approximation which depolarizes the reflected light completely. This is a realistic approximation as the largest polarized reflectances¹ observed by the PARASOL instrument over land are in the range between 0.02 and 0.04 (Maignan et al., 2009). The cloud fraction retrieval could work even without polarization produced by surface reflection because in the clear atmosphere, light is strongly polarized at 90° scattering angle due to Rayleigh scattering by molecules. Row (d) of Fig. 3 shows the simulations for a dark surface (albedo=0.0, scenario (d)). The blue line in the left figure shows the simulation for clear sky and we see the high degree of polarization around 90° scattering angle. When a cloud is added, the degree of polarization is smaller than for the corresponding cases over ocean, because the polarized reflectance from Rayleigh scattering is much smaller than from reflection in the sun glint. sun glint and the signal of the cloud dominates. The lookup-table plot shows that indicates that, for small cloud optical thicknesses and small cloud fractions the lines separate well but for high cloud optical thicknesses the lines move closer together, which would result in low cloud fractions, the lines are distinct, but as the cloud optical thickness increases, the lines converge. This convergence may lead to less accurate retrieval results given for the same measurement accuracy.

If the surface albedo is not 0 this becomes even nonzero, this situation becomes worse. Row (de) of Fig. 3 shows the results for a surface albedo of 0.2. In this case the surface depolarizes and the full lookup-table is squeezed entire lookup table is compressed making a retrieval impossible.

3.3 Dependence on various parameters, e.g. wind speed, aerosol properties, cloud microphysics

In order to test To assess the robustness of the retrieval method we performed additional sensitivity studies which are presented in Fig. 4. The base case for all simulations is defined as follows: ocean surface, cloud layer at 2-3 km altitude with an optical thickness of $\tau_c=5$, cloud droplet effective radius 10 μm , wind speed 5 m/s, aerosol optical thickness $\tau_a=0.1$, solar zenith angle 50°. Starting from the base case, one of the parameters is varied whereas all other parameters are kept constant. We also include results for a scattering angle of 110°, not in the maximum of the sun glint. The panels in the left column of Fig. 4 show the sensitivities for $P(40^\circ)$ - $P(140^\circ)$, the middle ones correspond to $P(110^\circ)$, and those in the right column show the corresponding sensitivities for are for $P(90^\circ)$. Blue lines correspond to the results for a clear atmosphere, purple lines are for fully cloudy pixels, and the other colors represent partially cloudy pixels.

In scenario (a) the cloud optical thickness τ_c is varied: as shown before $|P(40^\circ)-P(140^\circ)|$ decreases with increasing τ_c for all cloud fractions c . For $\tau_c \lesssim 4$, the lines corresponding to different cloud fractions separate whereas for larger τ_c , $P(40^\circ)$ $P(140^\circ)$ is almost independent of cloud fraction. For $P(110^\circ)$ and $P(90^\circ)$ saturates more quickly with increasing τ_c and the lines corresponding to different cloud fractions clearly separate.

¹In the solar principal plane the polarized reflectance is defined as $R_p = \frac{\pi Q}{E_0 \cos \theta_0}$, where E_0 is the extraterrestrial solar irradiance and θ_0 is the solar zenith angle.

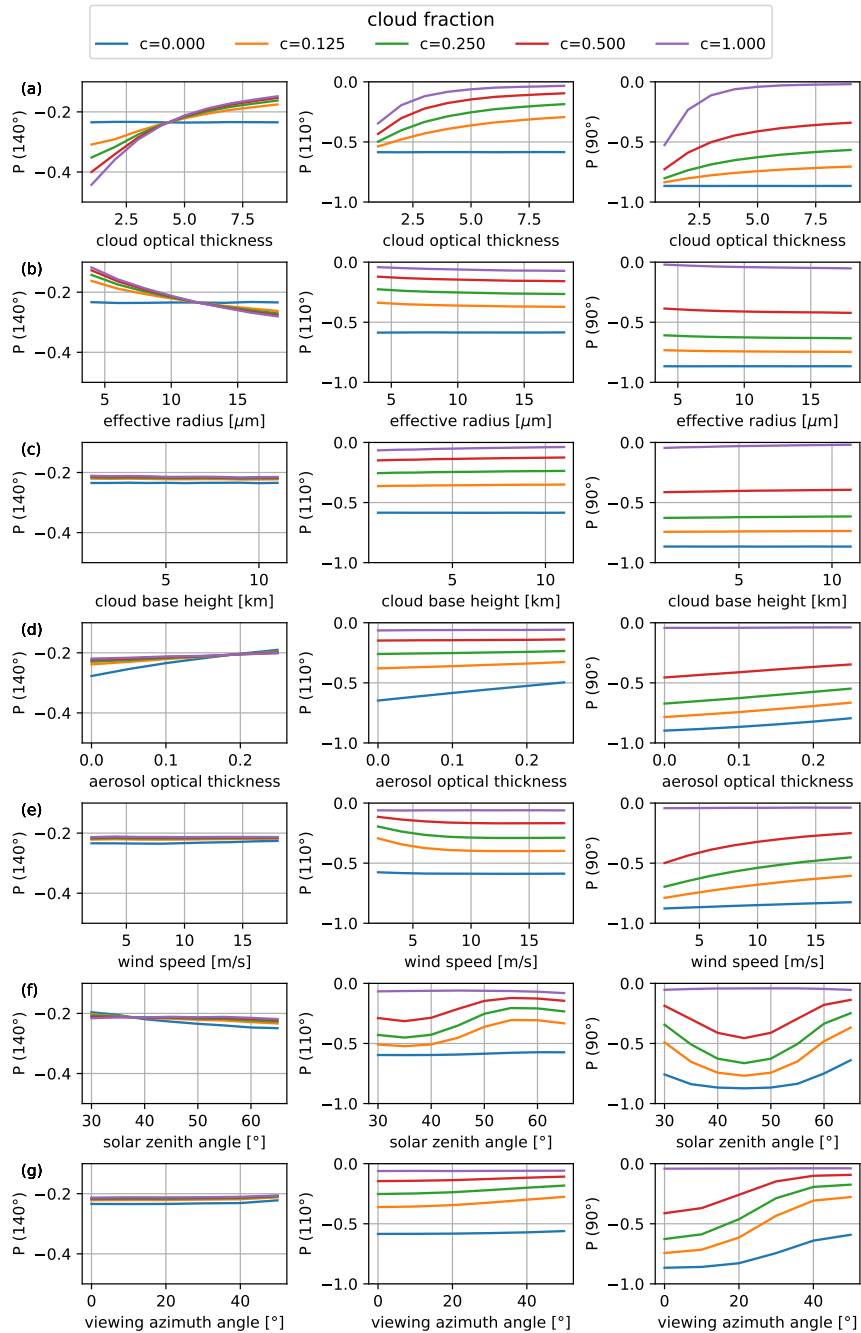


Figure 4. Dependencies of degree of polarization $P = Q/I$ at scattering angles of 140° (left), 110° (middle), and 90° (right) on cloud optical thickness, cloud droplet effective radius, cloud base height, aerosol optical thickness, wind speed, and solar zenith angle, and viewing azimuth angle. The colors correspond to cloud fractions between 0 and 1 (see legend). All simulations are for an ocean surface.

are clearly separated. In scenario (b) the droplet effective radius is varied: Here ~~$P(40^\circ)$~~ ~~decreases~~ ~~$P(140^\circ)$~~ increases with increasing effective radius. This implies that in order to retrieve an accurate optical thickness, the retrieval lookup table needs to be generated for the correct effective radius. ~~A way to realize this is~~ ~~Therefore, is makes sense~~ to combine the retrieval
310 with an effective radius retrieval based on the cloudbow signature. ~~$P(110^\circ)$ and $P(90^\circ)$~~ is-are almost independent of effective radius, therefore the cloud fraction retrieval does not require prior information on droplet size.

In scenario (c) the cloud top height is varied: ~~$P(40^\circ)$~~ , whereas the geometrical thickness of the cloud is kept constant at 1 km. ~~$P(140^\circ)$, $P(110^\circ)$~~ , and $P(90^\circ)$ are almost independent of cloud top height. This is a favorable outcome, suggesting that the retrieval process does not ~~need~~ necessitate prior information regarding cloud height.

top height. In scenario (d) the aerosol optical thickness is varied: ~~$P(40^\circ)$~~ ~~$P(140^\circ)$~~ remains constant, while ~~$P(110^\circ)$~~ and ~~$P(90^\circ)$~~ slightly decreases ~~decrease~~ with increasing aerosol optical thickness τ_a . These findings indicate that having prior information on τ_a would enhance the accuracy of the cloud fraction retrieval.

In scenario (e) the wind speed is varied: ~~$P(40^\circ)$~~ ~~$P(140^\circ)$~~ is not impacted by the sun-glint ~~sun-glint~~, therefore it is independent of wind speed. $P(90^\circ)$ is independent of wind speed for clear sky pixels and for fully cloudy pixels but not for partially cloudy
320 pixels. Therefore, prior information about wind speed from independent observations should be taken into account.

$P(110^\circ)$, at a scattering angle not in the center of the sun-glint, depends much less on the wind speed. This shows, that if there is no prior knowledge of wind speed, it may be better to use $P(110^\circ)$ instead of $P(90^\circ)$ although the polarization signal is weaker. In scenario (f) the solar zenith angle is varied: Again ~~$P(40^\circ)$~~ ~~$P(140^\circ)$~~ is constant but $P(90^\circ)$ ~~varies~~ and $P(110^\circ)$ vary, because the position of the glint depends on the solar zenith angle. The maximum of the glint is always at the mirror
325 reflection angle, i.e., it moves towards larger scattering angle as the solar zenith angle increases. For a solar zenith angle of 45° the ~~maximum of the sun-glint~~ maximum of the sun-glint is at 90° scattering angle. In scenario (g) the viewing azimuth angle is varied, which does not have an impact on $P(140^\circ)$. For $P(90^\circ)$ the impact is quite large, because as the viewing azimuth angle changes, the observing direction moves away from the center of the sun-glint. For $P(110^\circ)$ this dependence is much weaker, as the viewing direction is not close the center of the sun-glint.

330 In summary, the simulations suggest that the retrieval method is ~~anticipated to deliver highly expected to deliver~~ accurate cloud fractions and cloud optical thicknesses over the ocean, provided there is approximate prior information about wind speed and effective radius.

~~4 Application to airborne observations~~ Investigation of 3D scattering effects

In this section we apply the retrieval on polarized radiances obtained for the 3D model setups defined in Section 2.2.

335 4.1 2D scene with sharp cloud edge

Fig. 5 shows a sketch of the 2D cloud scene including relevant photon paths to explain the 3D effects. Photon 1 reaches the surface without interaction, then becomes highly polarized by reflection at the ocean surface and afterwards passes through the cloud towards the observer. From the observer's perspective there is a cloud in the field of view, but still the sun-glint

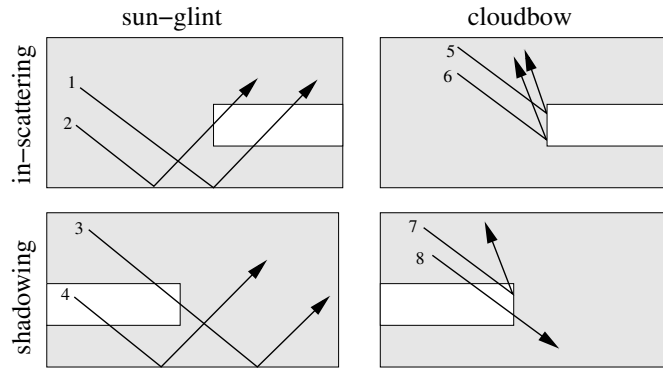


Figure 5. Sketch of individual photon paths to explain the basic 3D scattering effects.

polarization is partly visible. Photon 2 is similar, but the path through the cloud is shorter at the cloud edge, therefore the polarization is less decreased. Photons 3 and 4 pass the cloud and are reflected by the ocean surface towards the observer. However, much less photons will reach the surface directly compared to clear sky conditions, therefore from the observer's perspective, the degree of polarization in this clear sky pixel will be reduced. Photons 5 and 6 are scattered at the cloud side towards the observer at a scattering angle of 140° , i.e. in the cloudbow region. Due to the geometry of the cloud, additional photons are reflected at the cloud side towards the observer, which results in an increase in intensity and polarization at the cloud edge. For photons 7 and 8 the optical thickness of the cloud is reduced compared to a 1D layer, reducing the probability of scattering in the cloud. Photon 8 passes through the cloud and is eventually scattered in the atmosphere by a molecule.

Fig. 6 shows polarized radiances computed for the 2D cloud as defined in Section 2.2.1 for the in-scattering geometry. The upper panels are for a scattering angle of 140° (cloudbow) and the lower panels for a scattering angle of 90° (sun-glint). The simulations were performed at a spatial resolution of 500 m and averaged to obtain polarized radiances at a spatial resolution of 2.5 km (solid lines shown in Fig. 6). At the cloud edge we average over cloudy and clear-sky sub-pixels, this way we obtain results for cloud fractions of 1/5, 2/5, 3/5 and 4/5. The dashed lines show the corresponding 1D simulations where we combine clear-sky and cloudy simulation results using the IPA approximation (Eq. 7). In the cloudbow we find as expected an increase of the absolute values of I and Q close to the cloud edge compared to the 1D simulations (see photon paths 5 and 6 in Fig. 5). On the clear-sky side (0–10 km), the magnitude of the degree of polarization Q/I is decreased compared to 1D. On the cloudy side (10–20 km) it is increased, which means that the retrieval will underestimate the optical thickness. In the sun-glint, we find the most obvious differences for Q with much higher absolute values compared to the 1D simulations. This is due to photons that reach the surface directly on the clear side of the domain, are then reflected at the ocean surface and traverse the cloud towards the observer at the top of the atmosphere (see photon paths 1 and 2 in Fig. 5). For these cases the retrieval will underestimate the cloud fraction.

Fig. 7 presents the results for the cloud shadow geometry. Here the cloud is located between $x=0\text{km}$ and $x=10\text{km}$. In the cloudbow, the intensity I is decreased at the cloud edge compared to 1D approximations because the optical thickness is apparently smaller (compare photon paths 7 and 8 in Fig. 5). For Q the differences between 1D and 3D are relatively small.

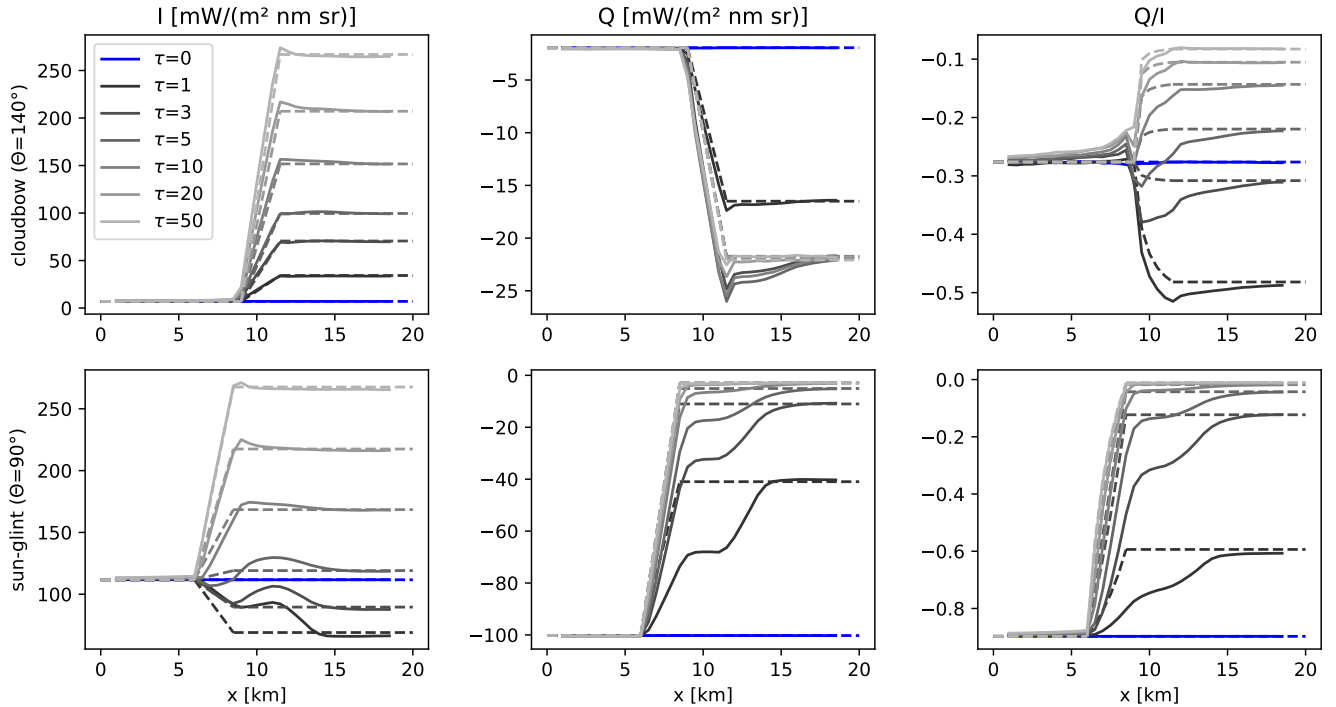


Figure 6. In-scattering results for sharp cloud edge: The solid lines show polarized radiances for in-scattering geometry averaged over a region of 2.5 km width. The upper row is for a scattering angle of 140° (cloudbow) and the lower row for a scattering angle of 90° (sun-glint). The dashed lines correspond to 1D simulations combined by the IPA approximation for partly cloud-covered pixels around the cloud edge. The blue lines corresponds to clear sky and the grey lines to cloudy simulations with various optical thicknesses between 1 and 50.

The magnitude of the degree of polarization is increased on the cloudy side and decreased on the clear side. In the sun-glint geometry we find very large differences between 3D and 1D simulations in the cloud shadow. Naturally, the intensity I is decreased in the cloud shadow compared to clear sky. The magnitude of the degree of polarization is much smaller in the cloud shadow which can be seen in Q and Q/I , obviously because photons cannot reach the surface directly (see photon paths 3 and 4 in Fig. 5). Due to the decreased degree of polarization the retrieval will detect clouds in the cloud shadow region.

Fig. 8 shows the retrieval lookup table derived in Section 3 including all results of the 3D simulations for the 2D step cloud. For better interpretation we mark all results obtained for in-scattering geometry as circles and all results obtained for shadowing geometry as squares. In the left panel, the colors of the points correspond to the cloud fraction of the region over which we have averaged (i.e., the input geometrical cloud fraction) and in the right panel the colors correspond to the vertical optical thickness of the cloud. We can check in these plots, for which of the points the retrieval is correct and where the retrieval does not work correctly, just by comparing the colors of the points to the colors of the lines in the lookup table plots. For the in-scattering, we see that fully cloud covered pixels (light blue circles) lie in the lookup-table between cloud fractions of 0.8 and 1.0. Dark

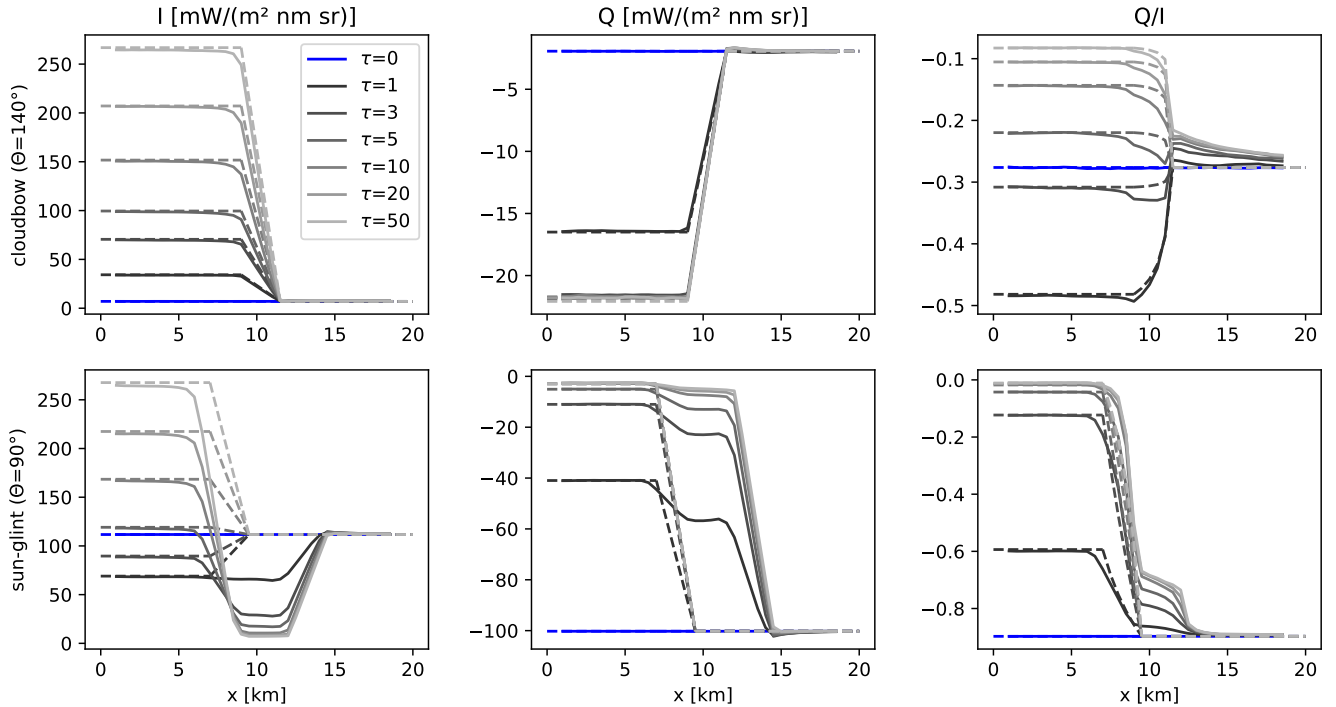


Figure 7. As Fig. 6 but for the cloud shadow geometry.

375 blue squares correspond to the points in the clear region, but many of those points lie on a vertical line along the $\tau=3$ isoline, these points correspond to simulations in the cloud shadow where a cloud is erroneously detected. The points corresponding to optical thickness of 1 (black points in right figure) lie outside the lookup table because in the cloudbow the magnitude of the degree of polarization in 3D is larger than in 1D, for in-scattering and shadowing.

380 Fig. 9 shows scatter plots of the retrieval. The left panel shows the retrieved cloud fraction versus the input cloud fraction (vertical geometrical cloud fraction). The blue lines correspond to the values obtained for the in-scattering geometry. As already discussed above, we find an underestimation of the cloud fraction, because in this geometry the degree of polarization for the 2D cloud scene is higher than for the corresponding 1D cloud layer. For the shadowing geometry (orange squares) the cloud fraction is overestimated because the degree of polarization is decreased in the shadow. Under- and overestimation can both become quite large for the extreme case of a sharp cloud edge. For example, for an input cloud fraction of 0.4, the retrieved

385 cloud fractions are in the range between 0.2 and 0.9. The right panel shows the scatter plot for the optical thickness retrieval. Here we filtered out the points for which the retrieved cloud fraction is smaller than 0.1, because for very small cloud fractions the retrieval becomes insensitive to optical thickness. Generally, we find a good correlation between input and retrieved optical thickness, but there is a significant bias towards too small retrieved optical thicknesses. This is the expected result, because we have seen for in-scattering and shadowing, that the absolute value of the degree of polarization is larger in the 3D results than

390 in the corresponding 1D results. The underestimation of the cloud optical thickness due to the neglect of 3D cloud scattering

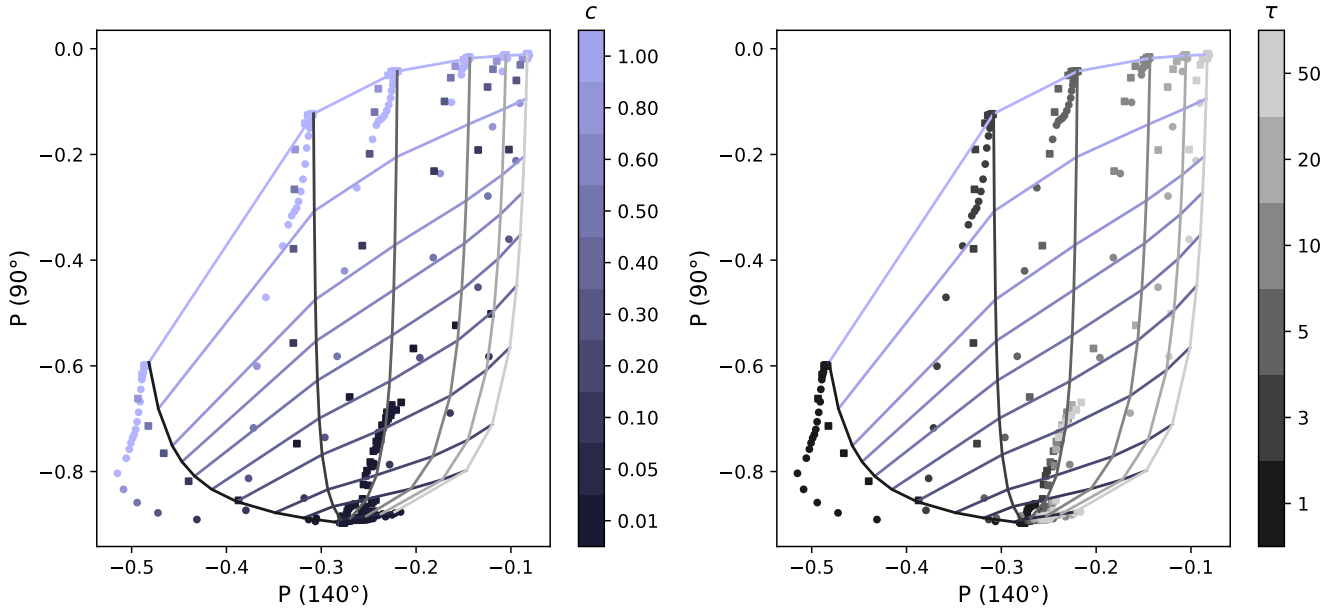


Figure 8. Retrieval lookup table derived in Section 3 including the results of the 3D simulations for the 2D cloud with sharp edge. Circles are for in-scattering and squares for shadowing. In the left panel the colors of the points correspond to the input cloud fraction and in the right panels the colors correspond to the input vertical optical thickness.

has also been observed for other cloud optical thickness retrieval methods (e.g., Zinner et al., 2010; Alexandrov et al., 2024). Note that we still look at the extreme case of a very sharp cloud edge, for which we expect very strong 3D scattering effects.

4.2 Randomly distributed box clouds

In the following, we present the results for the randomly distributed box clouds which shall resemble a shallow cumulus field (see Fig. 10). In the cloudbow, the intensity I is only weakly influenced by 3D scattering effects, i.e. the solid lines for the broken cloud fields lie on top of the dashed lines showing the IPA calculations. $|Q|$, which saturates quickly for $\tau \geq 3$, is slightly larger for 3D compared to IPA. This difference is enhanced in the degree of polarization shown in the right panels. In the sun-glint, the intensity I is smaller for 3D than for IPA due to cloud shadows. Note that the apparent noise of the curves is due to the random cloud field generation, not due to Monte Carlo noise, which is $< 1\%$. $|Q|$ is decreased significantly in 3D compared to 1D, also due to cloud shadowing. Since the effect of shadowing is the same for I and Q it partly cancels out in the degree of polarization, but still, $|P|$ is smaller in the 3D compared to 1D. This effect will cause a systematic overestimation of the retrieved cloud fractions.

Fig. 11 shows the retrieval lookup table including the results of the 3D simulations for the randomly distributed box clouds. The points corresponding to constant optical thickness values align next to the isolines of constant optical thickness, but shifted to the left. This shows again, that the neglect of 3D scattering yields an underestimation of cloud optical thickness. The colors of

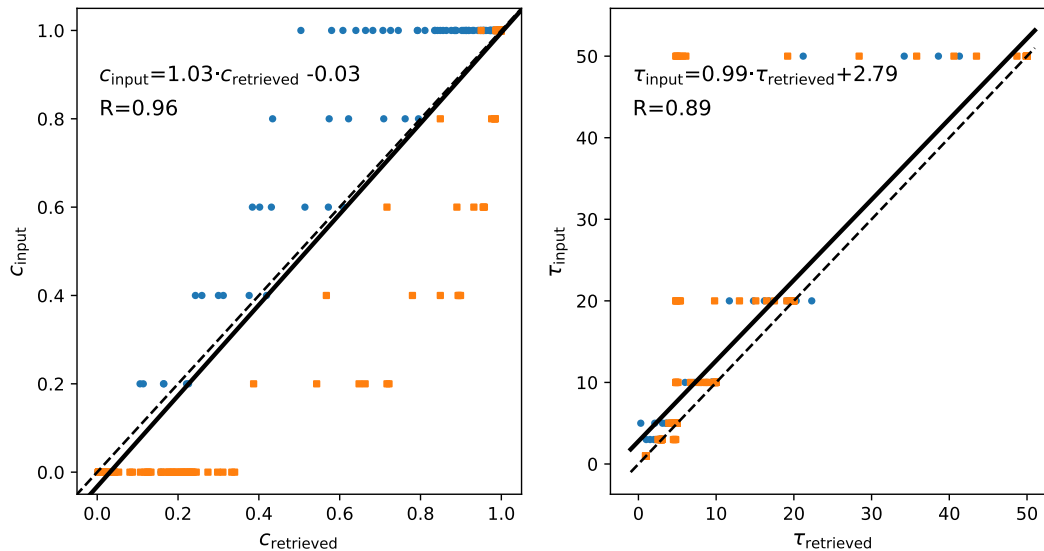


Figure 9. Scatter plots of the retrieved versus the input cloud fractions (left) and optical thicknesses (right). The blue circles correspond to in-scattering and the orange squares to shadowing. In the right panel points with a retrieved cloud fraction smaller than 0.1 have been filtered out. The solid black line shows the linear regression line and the dashed line is the one-one-line. The equation of the linear regression lines, and the correlation coefficients R are included in the figure.

the dots correspond to the geometrical cloud fraction of the model input. They roughly match the colors of the lines, indicating that the cloud fraction retrieval will yield reasonable results.

More quantitatively, Fig. 12 presents the retrieval results as scatter plots. The left panel shows the cloud fraction retrieval. As expected, we find a systematic overestimation of the retrieved cloud fraction, because the cloud shadows decrease the degree of polarization in the sun-glint region. The error becomes larger for larger input optical thicknesses as the colors of the dots indicate. Note that for our specific case of shallow broken cloud fields, we do not get an underestimation of cloud fraction due to in-scattering. The right panel shows the vertical optical thickness retrieval which is biased towards too small values, consistently with the cloud edge case. The underestimation increases with decreasing cloud fraction as indicated by the color of the dots in the right panel. There is one outlier for which the retrieved optical thickness is very small and the cloud fraction is then largely overestimated. Overall, we obtain a very good correlation between the retrieval results and the input data for both, the cloud fraction ($R=0.95$) and the cloud optical thickness ($R=0.99$).

5 Testing the retrieval method on high spatial resolution aircraft data

In this section we test the retrieval method using airborne observations taken by the ~~specMACS instrument spectrometer of the Munich Aerosol Cloud Scanner (specMACS)~~ on the HALO (High Altitude and Long Range research) aircraft during the ~~EUREC4A~~ EUREC⁴A (Elucidating the Role of Cloud-Circulation Coupling in Climate) measurement campaign.

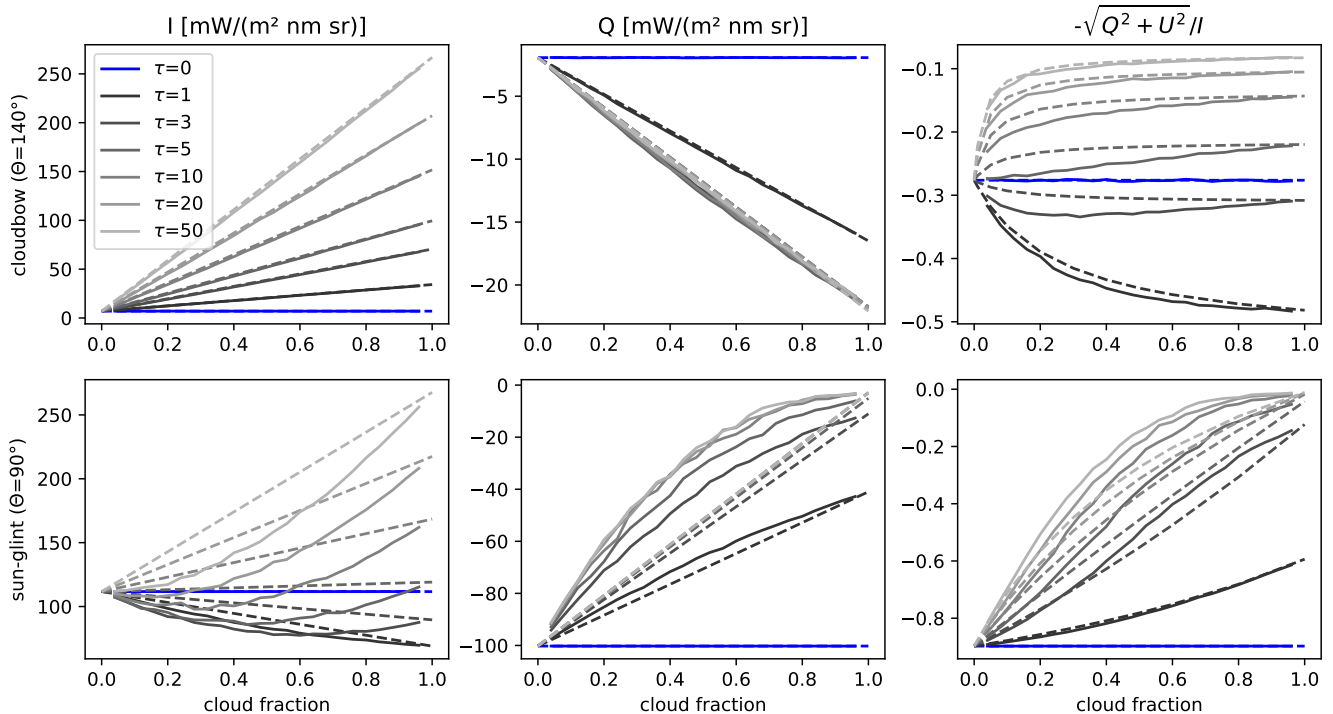


Figure 10. Polarized radiance (I and Q) and degree of polarization P as a function of cloud fraction. The solid lines are for randomly distributed box clouds and the dashed lines are IPA calculations. The spatial resolution of the individual grid boxes is 500 m^2 and the vertical geometrical thickness of the cloud boxes is 100 m .

5.1 Polarimetric observations with specMACS polarization cameras

The spectrometer of the Munich Aerosol Cloud Scanner (specMACS; Ewald et al., 2016) specMACS instrument (Ewald et al., 2016) consists of two hyperspectral line cameras covering the spectral range from 400 to 2500 nm and two identical polarization-sensitive imaging cameras (Pörtge et al., 2023) (Pörtge et al., 2023; Weber et al., 2023). The two polarization-sensitive cameras have a combined maximum field of view of about $\pm 45.91^\circ \times \pm 59.117^\circ$ (along track \times cross-track). This results in a horizontal pixel-size resolution of 10–20 m at ground when the flight altitude is around 10 km. The cameras take images at an acquisition frequency of 8 Hz. The sensors include on-chip directional polarizing filters which allow to measure the intensity and the linear polarization, i.e. the Stokes vector components I , Q , and U . These are geometrically (Kölling et al., 2019) and radiometrically calibrated (Weber et al., 2023). The central wavelengths (bandwidth) of specMaes bandwidths of the three channels of specMACS are approximately 621 nm (66 nm), 547 nm (117 nm) and 468 nm (82 nm). In the following we use data that were measured during the EUREC4A (EUropean Role of Cloud-Circulation Coupling in Climate) EUREC⁴A field campaign which took place in January and February 2020 with base in Barbados (Stevens et al., 2021). All observations during the EUREC4A EUREC⁴A campaign were taken over ocean.

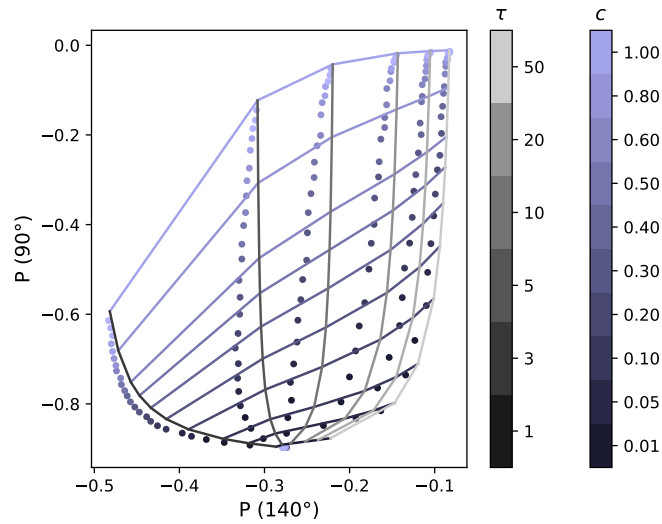


Figure 11. Lookup table including the results of the 3D simulations for the randomly distributed box clouds. The colors of the dots correspond to the input geometrical cloud fraction.

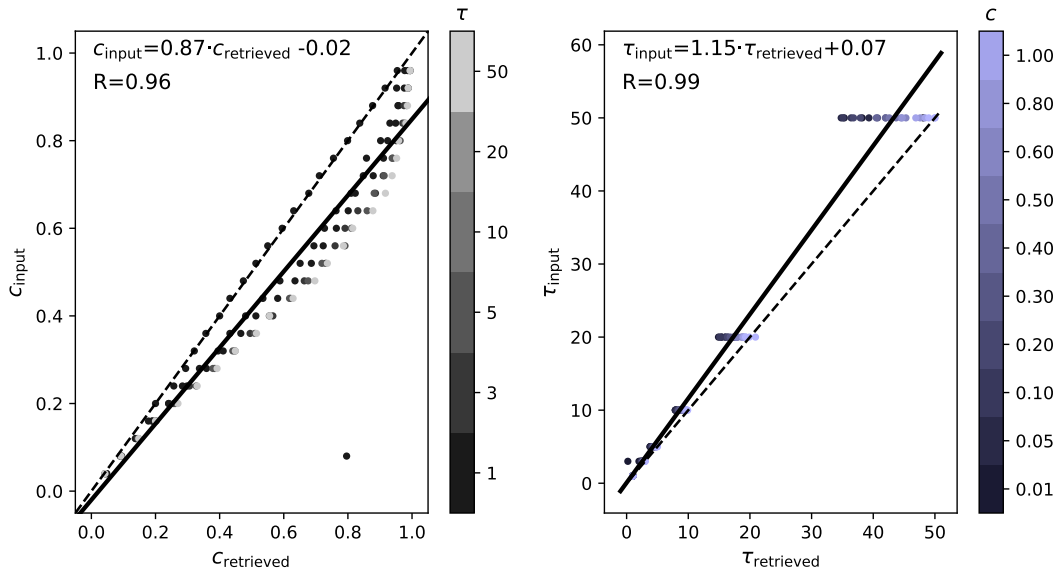


Figure 12. Retrieval results for randomly distributed shallow clouds. The left panel shows the cloud fraction retrieval. The color of the dots correspond to the input optical thickness. The right panel shows the optical thickness retrieval and the color of the dots correspond to the input cloud fraction. The solid black line shows the linear regression line and the dashed black lines are the 1:1 lines. The equation of the linear regression line, and the correlation coefficient R are included in the figures.

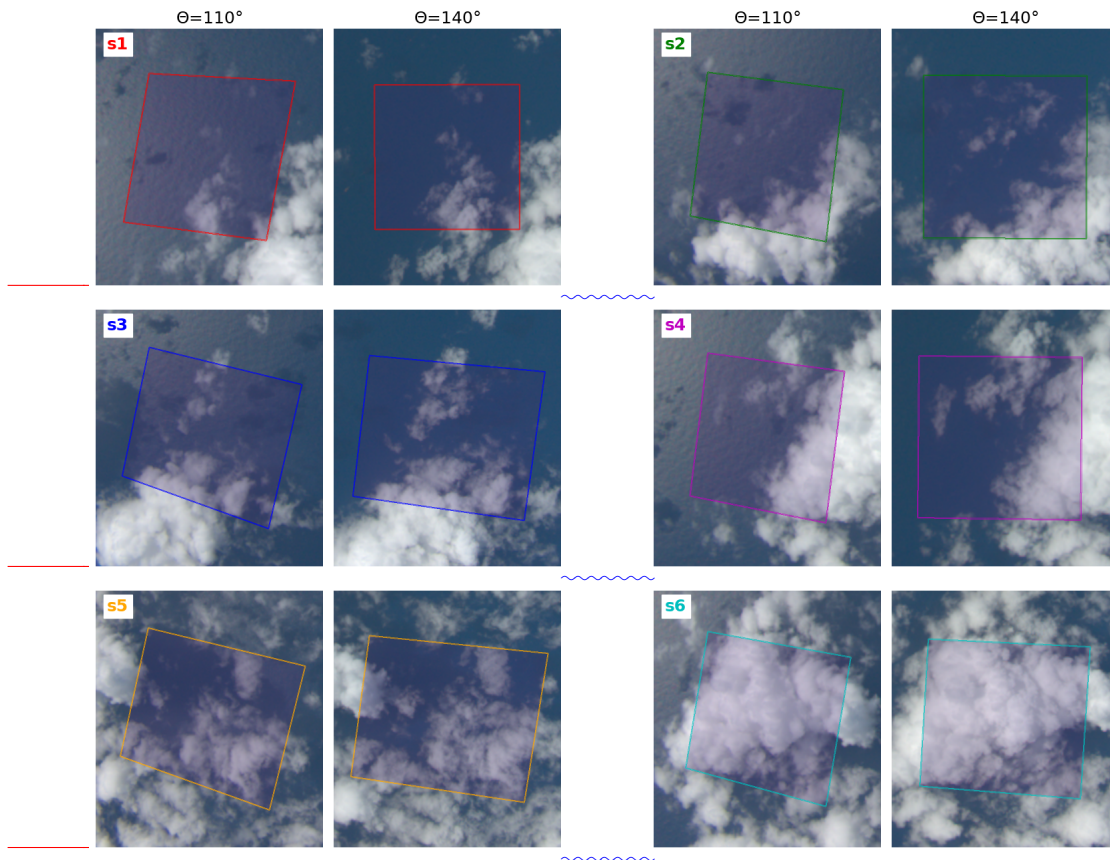


Figure 13. Six selected cloud scenes ~~s1–s6~~ s1 to s6 observed by ~~specMaes~~ specMACS over ocean. The size of the shaded area in each image is approximately $2.5 \times 2.5 \text{ km}^2$. For each of the scenes the cloud field is observed from different viewing directions during the overflight. In the left images of each scene, the average scattering angle over the shaded region is ~~70~~ 110° and in the right images it is ~~40~~ 140°.

We selected six scenes including shallow cumulus clouds observed on ~~28th–28th~~ 28th of January 2020. These contain various cloud fractions, from almost clear to almost fully cloud covered. The size of the scenes is approximately $2.5 \times 2.5 \text{ km}^2$ ~~corresponding equivalent~~ to the pixel size of, e.g. ~~HARPS~~, HARP2 and the spatial resolution of the data is approximately 10 m. ~~Images~~ The images corresponding to the selected scenes ~~s1–~~ to s6 are presented in Fig. 13, ~~the same where each~~ cloud scene is shown at scattering angles around ~~70~~ 110° (left) and at scattering angles around ~~40~~ 140° (right). Note that in the left images the ocean surface is clearly brighter than in the right images due to the sun-glint whereas the brightness of the clouds is similar in both images. Across an image the scattering angle is not constant. Since we require observations at particular scattering angles we use the geo-localization ~~of cloud targets~~ as described in Kölling et al. (2019) and Pörtge et al. (2023) in order to obtain all pixels in the chosen region for a given scattering angle. Pixels obtained using this method are averaged to get the Stokes vector of a selected scene for a given scattering angle. Combining all scattering angles results in the phase curves ~~for the selected scenes. These are shown~~ which are shown in Fig. 14 for the ~~selected scenes for the~~ red channel of ~~specMaes~~ centered

at 620 nm centered at 621 nm. The I and Q components of the Stokes vector look similar to the simulations shown

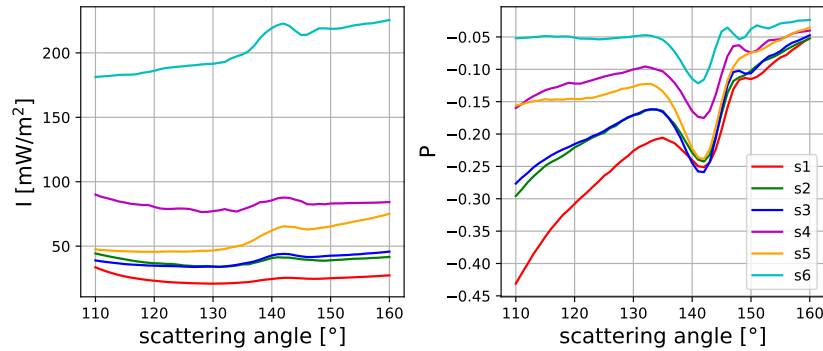


Figure 14. Phase curves of I and P observed by specMaes specMACS in the red channel centered at 620621 nm for the selected scenes which are shown in the images of Fig. 13.

445

in Fig. 1 in the scattering angle range between -75° and -20° . U is non-zero in the observational data because the viewing direction is not Since the observations are not taken exactly in the solar principal plane. Therefore we calculate the degree of polarization as follows:-

$$P = -\frac{\sqrt{Q^2 + U^2}}{I}$$

450

The minus sign indicates that the polarization direction is perpendicular to the scattering plane, i.e. P has the same sign as Q/I in the solar principal plane so that the curves can be compared to the U -component of the simulations shown in Section ?? Stokes vector becomes non-zero and we use Eq. 6 to calculate the signed degree of linear polarization. As expected we find that $|P|$ decreases with increasing cloud amount in the scenes (s1 is the scene including very few clouds and s5 and s6 are is almost fully cloud covered).

455

In order to retrieve cloud fraction and cloud optical thickness from specMACS data we generate a lookup table for the specific time and conditions when the observations were taken. We performed monochromatic simulations for the center wavelength of the red channel (621 nm). The solar zenith angle was 46.5° and we know that the total column aerosol optical thickness on the particular day was about 0.08 (measured by Veronika?) (Chazette et al., 2022). For simplicity we use a typical wind speed of 5 m/s and also, which is in agreement with Special Sensor Microwave Imager Sounder (SSMIS) observations

460

(Wentz et al., 2012). We also applied standard values for the water cloud droplet size distribution: an effective radius of $10 \mu\text{m}$ and an effective variance of 0.040.1. Results of the cloudbow retrieval (Pörtge et al., 2023) show that these values are realistic (compare Table 1). As we have shown in demonstrated in the sensitivity analysis in Section 3.2, inaccurate assumptions on cloud size cloud-size distribution parameters produce errors in the retrieval of cloud optical thickness while the cloud cover retrieval is not affected. much affected. For the selected scenes, we generated lookup-tables using the cloud size distribution

465

parameters from the cloudbow retrieval in addition. Of course, it would make sense to combine the method with further retrieval algorithms, e.g., with the simultaneous aerosol and ocean glint retrieval by Knobelspiesse et al. (2011). When accurate a priori

information about wind speed and aerosol optical thickness is included, one should also take into account the filter function of the instrument rather than running monochromatic simulations to generate the lookup-table. These improvements are not necessarily needed to demonstrate the method for a few specific cases, which is the purpose of this study. With specMACS we also can not obtain scattering angles of 40° and 90° for the same cloud-scene region, therefore we use 40° and 70° instead to generate the lookup table shown in Fig. 15. The lookup table based on 140° and 110° that we use for the specMACS data is slightly more tilted compared with the lookup table based on 140° and 90° that was mainly presented until here (Fig. 2). Nevertheless, the lookup table for the specMACS data still appears to be well suited to apply the method. The colored dots

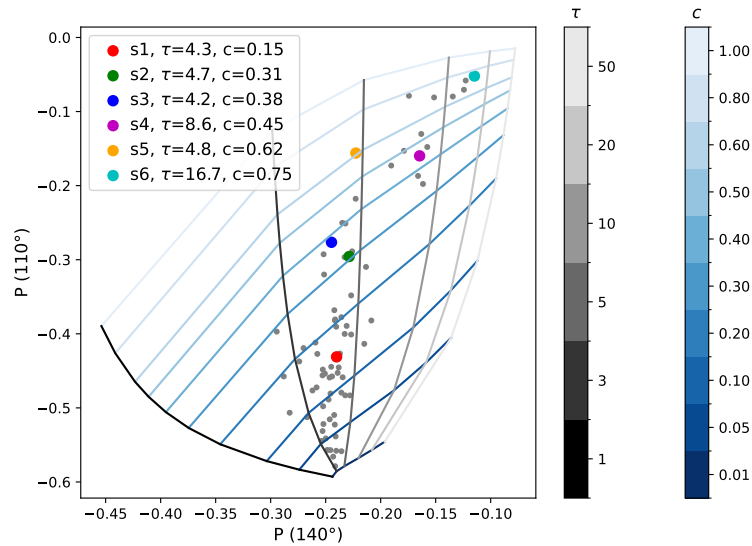


Figure 15. Retrieval lookup table and observational data. The colored dots represent the observed values of the six selected scenes shown in Fig. 13. The legend includes the retrieved optical thickness and cloud fraction values for those points. The grey dots are all data points gathered during one research flight on 28th-28th January 2020-2020 (observations averaged to 2.5 km spatial resolution).

plotted on top of the lookup table correspond to the observational data of the six selected scenes. The grey dots show all other data points that were measured with specMACS. Using a bi-linear interpolation between the simulated grid points of the lookup table we retrieve the values for cloud optical thickness τ and cloud fraction c as included in the legend of Fig. 15.

We also employed the cloud fraction-retrieval-detection method outlined in (Pörtge et al., 2023) Pörtge et al. (2023) on the images of the selected scenes -to determine the geometrical cloud fraction of the scenes at the original (high) resolution of the images. The method is based on intensity-thresholds-and-color-ratios-the algorithm described in Otsu (1979) which determines a threshold to separate the pixels of an image into two classes (here: cloudy versus non-cloudy) based on a brightness histogram. Such threshold based cloud detection algorithms often struggle with the bright sun-glint reflection. Our algorithm uses the parallel component of polarized light in which the reflectance of the sun-glint is reduced which in turn reduces the number of incorrect classifications in (clear-sky) sun-glint areas. The algorithm distinguishes between cloud-free, low to medium cloud

coverage, and high cloud coverage. For cloud-free scenes it uses the data of the blue channel, for scenes with low/medium cloud coverage the data of the red channel, and otherwise the normalized red (r) to blue (b) ratio ($nrbr = (b - r)/(b + r)$). This procedure was found by tuning the cloud mask for many different scenes (both over land and over water). Figure 16 shows two example measurements with contourlines of the calculated cloud mask in light-green. This figure illustrates that the algorithm correctly identifies the large cloud structures but misses some of the smaller and optically thinner clouds. Until now, the cloud detection method was mainly used to identify measurements that are suitable for the microphysical cloudbow retrieval of Pörtge et al. (2023). Therefore, the algorithm was tuned to minimize the amount of falsely classified clouds (e.g. due to the sun-glint).

The colored boxes in Fig. 16 indicate the positions of the six scenes ($s1$ to $s6$) from which the (pixel-based) cloud fraction is calculated. It should be noted that using this approach, the cloud fraction depends on the viewing angle but this dependence is relatively small for shallow clouds. Again, please note the difference between the two approaches: The threshold-based results correspond to a pixel-by-pixel cloud fraction and the lookup table allows a retrieval of the cloud fraction, which is independent of spatial resolution and does not rely on thresholds.

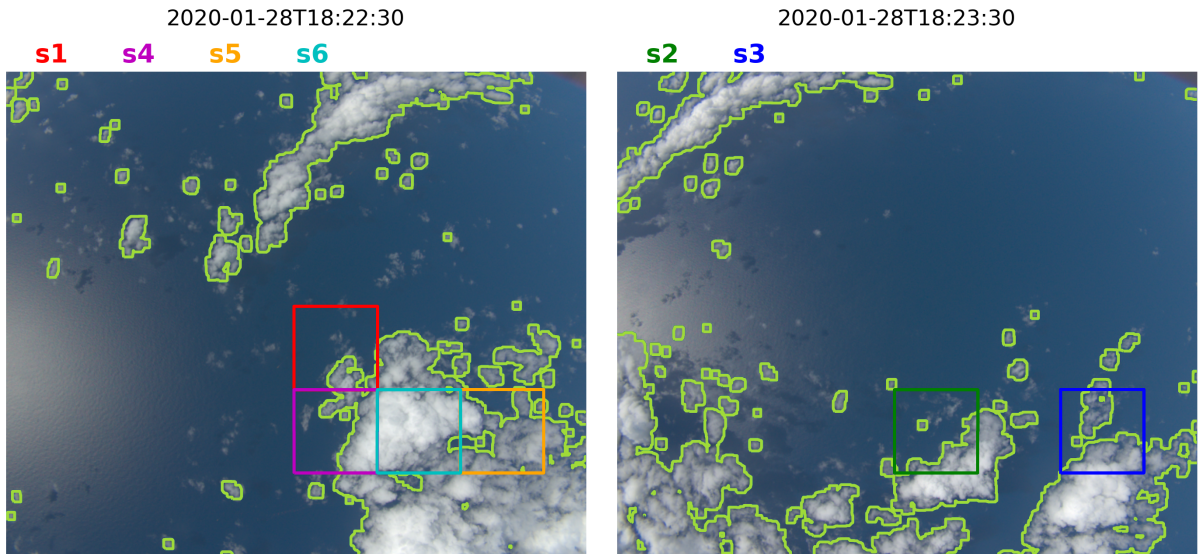


Figure 16. RGB images at two times (left: 18:22:30 and right: 18:23:30 UTC) with cloudmask as light-green lines. The regions of the selected scenes $s1$ to $s6$ are indicated as colored boxes.

Results for the selected scenes are included in Table 1): τ_1 and c_1 are the optical thickness and the cloud fraction obtained from the lookup-table retrieval using constant cloud size distribution parameters as input. τ_2 and c_2 are obtained when the retrieval is combined with the cloudbow retrieval, taking into account the retrieved effective radius r_{eff} and effective variance v_{eff} , which are also given in the table. c_3 is the (threshold-based) cloud fraction, which is defined as the ratio of the number of cloudy pixels and the total number of pixels in the high spatial resolution image. For scene $s1$ we obtain $\tau_1=2.4$ and $c_1=4.3$ and

$c_1=0.15$ from the lookup-table. The threshold-based retrieval algorithm in this case yields a higher cloud fraction of $c_1=0.37$ using constant cloud size distribution parameters. When the retrieved size distribution parameters from the cloudbow retrieval are used, the optical thickness is reduced to $\tau_1=0.37$. Comparing to the images in Fig. 13 the smaller cloud fraction seems more realistic and the cloud fraction is slightly increased to $c_2=0.17$. The threshold-based cloud fraction for this case is $c_3=0.15$, which agrees very well to the lookup-table based results. For scene s_2 the lookup table yields optical thicknesses of $\tau_1=4.6$ and $\tau_2=0.24$ which for this scene corresponds well to 4.4 and cloud fractions of $c_1=0.31$ and $c_2=0.33$, which are slightly larger than the threshold based cloud fraction $c_3=0.28$. For scene s_3 the threshold based retrieved value of cloud fraction is with $c_3=0.20$ and which looks reasonable when compared to the images. Scene s_4 includes partly the same clouds as scene s_2 much larger than for s_2 which is not so clearly visible when comparing the images in Fig. 13. Looking at the contours of the cloud mask in Fig. 16, we see that for s_3 a large region including thin clouds is marked as cloudy, whereas in s_2 but in addition a larger part of the thicker cloud as seen in the lower right part of the images. Consistently, we get for scene s_4 larger values for optical thickness (τ , several thin clouds are not detected. The lookup-table based cloud fraction values are smaller ($c_1=0.29$ and cloud cover ($c_1=0.38$ and $c_2=0.48$), corresponding well to threshold-based retrieval with $c_3=0.37$) and therefore only slightly larger than those derived for s_2 . The cloud optical thickness values ($\tau_1=0.45$. In scene s_3 the images show a clear area in the center surrounded by clouds from all directions. Although in the RGB image the sun glint is not well visible, the lookup-table based retrieval yields reasonable results of $\tau_1=4.2$ and $\tau_2=5.9$ and $c_3=0.45$) are also similar to s_2 . For s_4 , all retrieved cloud fractions agree well ($c_1=0.58$. Again the cloud fraction corresponds well to the threshold based retrieval with $c_3=0.45$, $c_2=0.54$. The last two scenes s_5 ($c_1=0.43$, and $c_3=0.43$). The optical thicknesses are larger than in the previous scenes ($\tau_1=8.6$ and s_6 include the same clouds which are slightly shifted from one scene to the next. The upper left part of scene s_5 ($\tau_2=9.1$). For scene s_5 is cloud free whereas scene s_6 is almost completely filled with clouds with some small gaps. The retrieved τ is therefore very similar in both scenes (τ the lookup-table retrievals yield the same cloud fraction of $c_{1,2}=0.175$ for s_5 and $\tau=0.62$. The threshold based cloud fraction is significantly higher with $c_3=0.77$. The cloud optical thickness for s_5 is relatively small ($\tau_1=16.9$ for s_6) whereas the cloud fraction is significantly larger for 4.8 and $\tau_2=4.7$). For all scenes discussed so far, the error due to the assumption of constant size distribution parameters was relatively small. This is different in the last scene s_6 as expected by looking at the images (e.g. for which the cloudbow retrieval yields a significantly larger effective radius of $14.5 \mu\text{m}$. Here, the retrieved optical thickness is almost doubled ($\tau_1=0.73$ for s_5 and $\tau=16.7$ and $\tau_2=0.86$ for s_6). For these two cases the threshold-based algorithm yields higher cloud fraction values ($c_3=0.31$) when the correct size distribution is used to generate the lookup table. The impact on the cloud fraction retrieval is relatively small ($c_1=0.99$ for s_5 and $c_1=0.75$ and $c_2=0.96$ for s_6), 0.70). The cloud detection algorithm classifies almost all pixels in s_6 as cloudy, resulting in a cloud cover of $c_3=0.98$. Looking at the images in Fig. 13 it seems that the algorithm does not detect the small gaps between thicker clouds as cloud free, there are some clear-sky areas in the lower right part of the images which are classified as cloudy by the cloud detection algorithm. However, visually the cloud fraction looks larger than 0.75, so we can not clearly conclude, which of the methods performs better for the specific scene s_6 .

The gray dots included in the lookup table in Fig. 15 correspond to all specMACS observations taken during a one hour period of the research flight on 28th of January 2020, 2020, for which the viewing azimuth angle is not more than 40°

retrieval method	$P(110)/P(140)$		$P(110)/P(140)$		cloud detection	cloudbow	
scene	τ_1	c_1	τ_2	c_2	c_3	r_{eff}	v_{eff}
s1	4.3	0.15	3.5	0.17	0.15	8.6	0.23
s2	4.7	0.31	4.4	0.33	0.28	9.7	0.22
s3	4.2	0.38	4.5	0.37	0.52	10.7	0.10
s4	8.6	0.45	9.1	0.43	0.43	10.7	0.09
s5	4.8	0.62	4.7	0.62	0.77	9.8	0.15
s6	16.7	0.75	31.1	0.70	0.98	14.5	0.06

Table 1. Retrieval results for the selected scenes. τ_1 and c_1 are the cloud optical thickness and the cloud fraction derived from the degree of linear polarization at 110° and 140° assuming constant values of $r_{\text{eff}}=10 \mu\text{m}$ and $v_{\text{eff}}=0.01$. τ_2 and c_2 correspond to retrieval results taking into account r_{eff} and v_{eff} from the cloudbow retrieval (last two columns). c_3 is the fraction of cloudy pixels in the scene which is determined using a cloud detection algorithm on the high spatial resolution data.

away from the principal plane, making sure that the sun-glint is contained. In this range, $P(110)$ does not depend much on viewing azimuth angle (compare Fig. 4). All dots are within the lookup table grid which means that the retrieval yields values for each observation. The retrieved cloud fractions and optical thicknesses are shown as histograms in Fig. 17. The

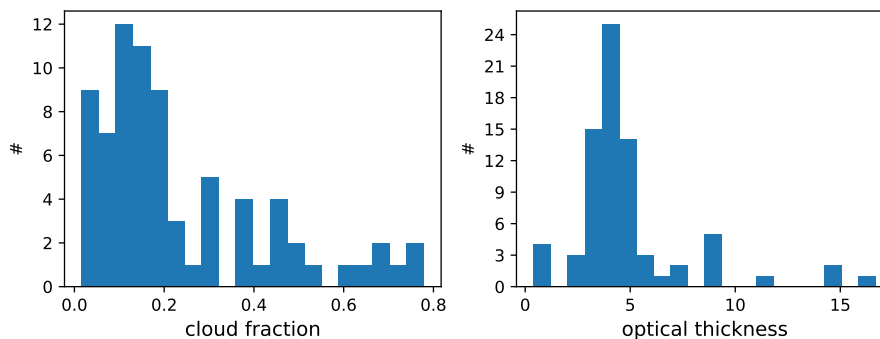


Figure 17. Histogram of retrieved cloud fractions and optical thicknesses using the lookup table method.

540 ~~EUREC4A-EUREC⁴A~~ campaign focused on shallow cumulus clouds which were also observed on 28th of January 2020. The optical thickness of this type of clouds is usually quite small which can also be seen in the cloud optical thickness histogram that we obtain for the particular flight, showing an optical thickness below 10 for the majority of the points. ~~The horizontal extent of the clouds can several kilometers, therefore we find all~~ A large range of cloud fraction values between 0 and 1, depending on the exact location of the selected ~~0.8 is covered by the observations when the cloud detection algorithm is~~ 545 ~~evaluated over areas of $2.5 \times 2.5 \text{ km}^2$ large scenes.~~ The majority of points has relatively low cloud fractions ~~below smaller than~~ 0.2. In Fig. 18, the retrieved cloud fractions obtained through the lookup-table method are plotted on the x -axis versus the

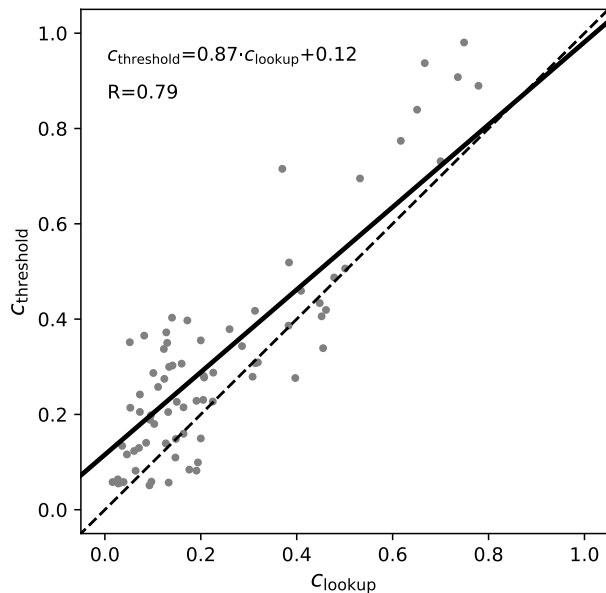


Figure 18. Cloud-Scatter plot of the retrieved cloud fractions: C_{lookup} is the cloud fraction derived by the lookup table method versus cloud fractions derived using a combined threshold and color from the polarized reflectance at two viewing angles. $C_{threshold}$ is the ratio method of cloudy pixels to the total number of pixels within an area of size 2.5×2.5 km² contained in a specMACS image with a spatial resolution of about 10 m. The equation of the linear regression line (black line) is included in the figure together with the regression coefficient R .

retrieved cloud fraction-fractions obtained through the threshold method on the y -axis. The linear regression line has a slope of 0.91~~0.87~~, and the correlation coefficient is 0.87. ~~Specifically, within the high cloud fraction regime, the~~ 0.79. The scatter plot demonstrates that the threshold-based retrieval often results in larger cloud fractions compared to the lookup table-based retrieval, a pattern consistently observed in the selected scenes $s5$ and $s6$. ~~Conversely, in the low cloud fraction regime, the lookup table method frequently produces higher values than the threshold method.~~ The strong correlation underscores confirms that the straightforward and robust lookup table retrieval method provides reasonable cloud fraction values for the entire flight's observations.

6 Conclusions and Outlook

555 We have presented an innovative and straightforward approach to retrieve cloud fraction and optical thickness from multi-angle polarization observations over ocean. This retrieval method could be a valuable addition ~~for instance,~~ for instance, to the cloud retrieval chain for the PACE mission including the polarimeters HARPS and SpexOne~~HARP2 and SPEXone~~. Here it should be combined with other retrieval methods to obtain required a priori information on aerosol optical thickness, wind speed, and cloud droplet size distribution. Given the typical spatial resolution of upcoming polarized satellite-based measurements ~~of~~ of 560 approximately 2-3 km, this technique becomes particularly valuable for acquiring sub-pixel information about clouds.

565 Unlike most other cloud fraction retrieval methods, our approach does not depend on the spatial resolution of the observations and it also does not require any thresholds for cloud detection. The fundamental principle of this method lies in the distinctive angular polarization patterns generated by the interaction of radiation with various components of the Earth's atmosphere-surface system the liquid water clouds and water surface. Specifically, cloud scattering generates polarization at cloud-bow cloudbow scattering angles, while ocean surface reflection results in the strongly polarized sun-glint around the mirror reflection angle. Consequently, by analyzing the angular polarization pattern, we can effectively separate the contributions of clouds and the surface to the observed polarized intensity.

570 Our sensitivity study reveals that the complete angular pattern of polarized intensity is not required. Instead, two specific scattering angles – one within the cloudbow and one within the sun-glint – prove to be are sufficient. Utilizing a 1D vector radiative transfer code, we generated the retrieval lookup tables that incorporate include the simulated degree of polarization at 40 140° and 90° scattering angles for various cloud optical thicknesses between 0 and 50. To calculate polarized intensities for partially cloudy pixels we employ the independent pixel approximation. When we plot the degree of polarization at 40° scattering angle against the degree of polarization at 90° We also generated lookup tables using scattering angles of 140° scattering angle and connect data points of constant optical thickness and data points of constant cloud cover, we obtain 575 and 110° and again obtained a well-separated lines, forming an almost rectangular lookup table grid. lookup table grid. This demonstrates, that it is not important to choose exact scattering angles to set up the retrieval, one only has to make sure, that one angle includes the cloudbow and the second angle a part of the sun-glint.

580 We examined the influence of cloud droplet size, cloud top height, aerosol optical thickness, and wind speed on the retrieval accuracy. We found that the retrieval results are almost independent of cloud top height. The cloud fraction retrieval slightly slightly depends on aerosol optical thickness and on wind-speed wind speed, therefore prior knowledge on these parameters is advantageous. The retrieval of cloud optical thickness depends on droplet radius. Hence, deriving this parameter, for instance, through methods like the cloudbow retrieval, can significantly enhance accuracy.

585 We validated investigated the impact of 3D cloud scattering by generating synthetic observations for simple cloud cases. The first is a 2D scene, which is clear in one half of the domain and cloudy in the other half. At such a sharp cloud edge we expect strong 3D effects, shadowing on one side and in-scattering on the other side. We find that shadowing leads to a systematic overestimation of the cloud fraction, whereas in-scattering leads to a systematic underestimation. The cloud optical thickness is generally underestimated due to the neglect of 3D cloud scattering. In a second setup, we generated random cloud fields consisting of box clouds with various cloud fractions. This setup resembles a shallow cumulus cloud field and it allows us to systematically investigate the impact of 3D cloud scattering as a function of cloud cover. For this setup we found 590 that the retrieval systematically overestimates the cloud fraction and underestimates the cloud optical thickness, similar to the cloud edge case. The cloud fraction underestimation is not observed in this scenario. The value of the bias depends on many characteristics of the cloud field, in particular the horizontal and vertical distribution of the clouds. In addition, the geometrical thickness of the clouds plays a significant role since it directly determines the size of the cloud shadows.

595 We tested the method using specMACS observations conducted aboard the HALO aircraft during the EUREC4A EUREC4A campaign, focusing on shallow cumulus clouds over the ocean. Operating at a high spatial resolution of approximately 10-20 m,

specMACS data was averaged over domains of approximately $2.5 \times 2.5 \text{ km}^2$ to emulate satellite observations. Subsequently, the retrieval ~~algorithm method~~ was applied to the resulting degree of polarization at scattering angles of 40° and 70° . ~~We used 70° instead of 90° , because the specMACS data does not include the same cloud scene at 40° and 90° .~~ The retrieved optical thicknesses were typically below 10, ~~a~~ realistic range for the observed cloud type, and ~~all possible cloud fractions~~ ~~cloud fractions in the range~~ between 0 and ~~± 0.8~~ were retrieved. We selected six scenes, representing low, medium, and high cloud fractions. We analyzed the ~~accompanying~~ high-resolution images ~~, verifying the visual to visually verify the~~ consistency between the retrieved cloud fraction and the ~~content of the images. Remarkably, for all selected scenes, the retrieved cloud fractions consistently aligned with visual expectations. images.~~ Additionally, we applied another cloud fraction retrieval method based on ~~intensity thresholds and color ratios (Poertge et al., 2023).~~ ~~We observed a significant (automatically determined)~~ ~~intensity thresholds (Pörtge et al., 2023; Otsu, 1979). We find a good~~ correlation between the results of the two cloud fraction retrieval methods, providing further evidence of the ~~effectiveness performance~~ of the straightforward lookup-table retrieval approach.

In a subsequent study, we intend to further evaluate the accuracy of the retrieval ~~algorithm method~~ using synthetic data. ~~This data will be generated using the 3D vector radiative transfer code MYSTIC based on more realistic clouds generated using a~~ ~~Large Eddy Simulation (LES).~~ As we know the true optical thicknesses and cloud fractions for the synthetic dataset, assessing the retrieval accuracy becomes straightforward by comparing the obtained results with the model input. This approach will enable us to quantify the effects of 3D cloud scattering, including in-scattering and shadowing, on the retrieval results. ~~We have successfully applied this methodology to validate the accuracy of the cloud microphysics retrieval (Volkmer et al., 2023) and to investigate the impact of 3D cloud scattering on trace gas retrievals (Emde et al., 2022; Yu et al., 2022; Kylling et al., 2022).~~ ~~In this paper we have presented 3D effects based on simplified cloud scenes. For the case with the cloud edge, we found large underestimations of the cloud fractions on the in-scattering side and large overestimations on the shadowing side. Realistic cloud scenes include shadowing and in-scattering simultaneously and it should be investigated, to which extent these two effects cancel.~~

~~The methodology could be applied to the satellite observations, e.g. HARP2 data. The cloud fraction retrieval should be compared to the obtained pixel-by-pixel cloud fraction of images captured by the OCI instrument onboard PACE, which operates at a higher spatial resolution of $1.2 \times 1.2 \text{ km}^2$. When applied to satellite observations, it also needs to be investigated for which regional coverage measurements at scattering angles in cloudbow and glint can be delivered nearly simultaneously.~~

~~The derived cloud fraction of shallow cumulus clouds over ocean should be compared to the results by Dutta et al. (2020), who found cloud fraction reductions of more than 0.4 when the spatial resolution error is corrected. For climate and weather model validation, the global cloud fraction is an important quantity. The method we have presented provides the cloud fraction only for liquid water clouds over the ocean. Therefore our method needs to be adapted for ice clouds, which should be relatively straightforward by replacing the degree of polarization in the cloudbow by the intensity at a scattering angle outside the sun-glint region. The development of a cloud fraction retrieval over land surfaces is more challenging because land surface reflection causes only weak polarization. However, the Rayleigh scattering in clear regions between the clouds produces a~~

630 strong polarization signal that should contain information about the cloud fraction and could be used similarly to the glint polarization in the retrieval method presented here.

Author contributions. CE performed the sensitivity studies, set up the retrieval method, performed the tests on specMACS observations, and wrote the manuscript. VP provided the specMACS data. MM and BM helped to set up and improve the retrieval methodology. All authors contributed to the interpretation of the results and helped to improve the manuscript.

635 *Competing interests.* The contact author has declared that none of the authors has any competing interests.

Acknowledgements. ~~TEXT~~ We thank the two anonymous reviewers for valuable comments that helped to improve the manuscript.

References

- Alexandrov, M. D., Cairns, B., Emde, C., Ackerman, A. S., and van Diedenhoven, B.: Accuracy assessments of cloud droplet size retrievals from polarized reflectance measurements by the research scanning polarimeter, *Remote Sensing of Environment*, 125, 92 – 111, 2012.
- 640 Alexandrov, M. D., Cairns, B., Emde, C., and Van Diedenhoven, B.: Correction of cloud optical thickness retrievals from nadir reflectances in the presence of 3D radiative effects. Part I: concept and tests on 3D RT simulations, *FRONTIERS IN REMOTE SENSING*, 5, <https://doi.org/10.3389/frsen.2024.1397631>, 2024.
- Anderson, G., Clough, S., Kneizys, F., Chetwynd, J., and Shettle, E.: AFGL atmospheric constituent profiles (0-120 km), *Tech. Rep. AFGL-TR-86-0110*, Air Force Geophys. Lab., Hanscom Air Force Base, Bedford, Mass., 1986.
- 645 Bréon, F.-M. and Doutriaux-Boucher, M.: A comparison of Cloud Droplet Radii Measured from Space, *IEEE Transactions on Geoscience and Remote Sensing*, 43, 1769–1805, 2005.
- Buras, R. and Mayer, B.: Efficient unbiased variance reduction techniques for Monte Carlo simulations of radiative transfer in cloudy atmospheres: The solution, *J. Quant. Spectrosc. Radiat. Transfer*, 112, 434–447, 2011.
- Chandrasekhar, S.: *Radiative Transfer*, Oxford Univ. Press, UK, 1950.
- 650 Chazette, P., Baron, A., and Flamant, C.: Mesoscale spatio-temporal variability of airborne lidar-derived aerosol properties in the Barbados region during EUREC⁴A, *Atmospheric Chemistry and Physics*, 22, 1271–1292, <https://doi.org/10.5194/acp-22-1271-2022>, 2022.
- Cox, C. and Munk, W.: Measurement of the roughness of the sea surface from photographs of the sun's glitter, *Journal of the Optical Society of America*, 44, 838–850, 1954a.
- Cox, C. and Munk, W.: Statistics of the sea surface derived from sun glitter, *Journal of Marine Research*, 13, 198–227, 1954b.
- 655 Di Girolamo, L. and Davies, R.: Cloud fraction errors caused by finite resolution measurements, *Journal of Geophysical Research: Atmospheres*, 102, 1739–1756, <https://doi.org/https://doi.org/10.1029/96JD02663>, 1997.
- Dutta, S., Di Girolamo, L., Dey, S., Zhan, Y., Moroney, C. M., and Zhao, G.: The Reduction in Near-Global Cloud Cover After Correcting for Biases Caused by Finite Resolution Measurements, *Geophysical Research Letters*, 47, e2020GL090313, <https://doi.org/https://doi.org/10.1029/2020GL090313>, e2020GL090313 2020GL090313, 2020.
- 660 Emde, C., Buras, R., Mayer, B., and Blumthaler, M.: The impact of aerosols on polarized sky radiance: model development, validation, and applications, *Atmos. Chem. Phys.*, 10, 383–396, 2010.
- Emde, C., Barlakas, V., Cornet, C., Evans, F., Korokin, S., Ota, Y., Labonnote, L. C., Lyapustin, A., Macke, A., Mayer, B., and Wendisch, M.: IPRT polarized radiative transfer model intercomparison project - Phase A, *J. Quant. Spectrosc. Radiat. Transfer*, 164, 8–36, <https://doi.org/10.1016/j.jqsrt.2015.05.007>, 2015.
- 665 Emde, C., Buras-Schnell, R., Kylling, A., Mayer, B., Gasteiger, J., Hamann, U., Kylling, J., Richter, B., Pause, C., Dowling, T., and Bugliaro, L.: The libRadtran software package for radiative transfer calculations (version 2.0.1), *Geophys. Mod. Dev.*, 9, 1647–1672, <https://doi.org/10.5194/gmd-9-1647-2016>, 2016.
- Emde, C., Barlakas, V., Cornet, C., Evans, F., Wang, Z., Labonotte, L. C., Macke, A., Mayer, B., and Wendisch, M.: IPRT polarized radiative transfer model intercomparison project – Three-dimensional test cases (phase B), *J. Quant. Spectrosc. Radiat. Transfer*, 209, 19–44, <https://doi.org/10.1016/j.jqsrt.2018.01.024>, 2018.
- 670 Emde, C., Yu, H., Kylling, A., van Roozendaal, M., Stebel, K., Veihelmann, B., and Mayer, B.: Impact of 3D cloud structures on the atmospheric trace gas products from UV–Vis sounders – Part 1: Synthetic dataset for validation of trace gas retrieval algorithms, *Atmospheric Measurement Techniques*, 15, 1587–1608, <https://doi.org/10.5194/amt-15-1587-2022>, 2022.

- Ewald, F., Kölling, T., Baumgartner, A., Zinner, T., and Mayer, B.: Design and characterization of specMACS, a multipurpose hyperspectral
675 cloud and sky imager, *Atmospheric Measurement Techniques*, 9, 2015–2042, <https://doi.org/10.5194/amt-9-2015-2016>, 2016.
- Fougnie, B., Marbach, T., Lacan, A., Lang, R., Schlüssel, P., Poli, G., Munro, R., and Couto, A. B.: The multi-viewing multi-channel
multi-polarisation imager – Overview of the 3MI polarimetric mission for aerosol and cloud characterization, *Journal of Quantitative
Spectroscopy and Radiative Transfer*, 219, 23–32, <https://doi.org/10.1016/j.jqsrt.2018.07.008>, 2018.
- Hansen, J. E. and Hovenier, J. W.: Interpretation of the Polarization of Venus, *J. Atmos. Sci.*, 31, 1137 – 1160,
680 [https://doi.org/https://doi.org/10.1175/1520-0469\(1974\)031<1137:IOTPOV>2.0.CO;2](https://doi.org/https://doi.org/10.1175/1520-0469(1974)031<1137:IOTPOV>2.0.CO;2), 1974.
- Hansen, J. E. and Travis, L. D.: Light scattering in planetary atmospheres, *Space Science Reviews*, 16, 527–610, 1974.
- Hasekamp, O. P.: Capability of multi-viewing-angle photo-polarimetric measurements for the simultaneous retrieval of aerosol and cloud
properties, *Atmospheric Measurement Techniques*, 3, 839–851, <https://doi.org/10.5194/amt-3-839-2010>, 2010.
- Hess, M., Koepke, P., and Schult, I.: Optical Properties of Aerosols and Clouds: The Software Package OPAC, *Bulletin of the American
685 Meteorological Society*, 79, 831–844, 1998.
- Intergovernmental Panel On Climate Change: Technical Summary, in: *Climate Change 2013 – The Physical Science Basis*, pp. 31–116,
Cambridge University Press, 1 edn., <https://doi.org/10.1017/CBO9781107415324.005>, 2014.
- Intergovernmental Panel On Climate Change: *Climate Change 2021 – The Physical Science Basis: Working Group I Contribu-
tion to the Sixth Assessment Report of the Intergovernmental Panel on Climate Change*, Cambridge University Press, 1 edn.,
690 <https://doi.org/10.1017/9781009157896>, 2023.
- Knobelspiesse, K., Cairns, B., Redemann, J., Bergstrom, R. W., and Stohl, A.: Simultaneous retrieval of aerosol and cloud properties during
the MILAGRO field campaign, *Atmospheric Chemistry and Physics*, 11, 6245–6263, <https://doi.org/10.5194/acp-11-6245-2011>, 2011.
- Kölling, T., Zinner, T., and Mayer, B.: Aircraft-based stereographic reconstruction of 3-D cloud geometry, *Atmospheric Measurement Tech-
niques*, 12, 1155–1166, <https://doi.org/10.5194/amt-12-1155-2019>, 2019.
- 695 Kurucz, R. and Bell, B.: CD Rom No. 23, *Smithsonian Astrophys. Obs.*, extraterrestrial solar spectrum from 200–200000 nm, 1995.
- Kylling, A., Emde, C., Yu, H., van Roozendaal, M., Stebel, K., Veißelmann, B., and Mayer, B.: Impact of 3D cloud structures on the atmo-
spheric trace gas products from UV–Vis sounders – Part 3: Bias estimate using synthetic and observational data, *Atmospheric Measurement
Techniques*, 15, 3481–3495, <https://doi.org/10.5194/amt-15-3481-2022>, 2022.
- Maignan, F., Bréon, F.-M., Fédèle, E., and Bouvier, M.: Polarized reflectances of natural surfaces: Spaceborne measurements and analytical
700 modeling, *Remote Sensing of Environment*, 113, 2642–2650, <https://doi.org/10.1016/j.rse.2009.07.022>, 2009.
- Mayer, B.: Radiative transfer in the cloudy atmosphere, *European Physical Journal Conferences*, 1, 75–99, 2009.
- Mayer, B. and Kylling, A.: Technical note: The libRadtran software package for radiative transfer calculations – description and examples of
use, *Atmos. Chem. Phys.*, 5, 1855–1877, 2005.
- Mie, G.: Beiträge zur Optik trüber Medien, speziell kolloidaler Metallösungen, *Annalen der Physik*, 330, 377–445,
705 <https://doi.org/10.1002/andp.19083300302>, 1908.
- Mishchenko, M. I. and Travis, L. D.: Satellite retrieval of aerosol properties over the ocean using polarization as well as intensity of reflected
sunlight, *J. Geophys. Res.*, 102, 16 989–17 013, 1997.
- Nakajima, T. and King, M. D.: Determination of the optical thickness and effective particle radius of clouds from reflected solar radiation
measurements. Part I: theory, *Journal of the Atmospheric Sciences*, 47, 1878–1893, 1990.
- 710 Otsu, N.: A Threshold Selection Method from Gray-Level Histograms, *IEEE Transactions on Systems, Man, and Cybernetics*, 9, 62–66,
<https://doi.org/10.1109/TSMC.1979.4310076>, 1979.

- Platnick, S., Meyer, K. G., King, M. D., Wind, G., Amarasinghe, N., Marchant, B., Arnold, G. T., Zhang, Z., Hubanks, P. A., Holz, R. E., Yang, P., Ridgway, W. L., and Riedi, J.: The MODIS Cloud Optical and Microphysical Products: Collection 6 Updates and Examples From Terra and Aqua, *IEEE Transactions on Geoscience and Remote Sensing*, 55, 502–525, <https://doi.org/10.1109/TGRS.2016.2610522>, 2017.
- 715 Pörtge, V., Kölling, T., Weber, A., Volkmer, L., Emde, C., Zinner, T., Forster, L., and Mayer, B.: High-spatial-resolution retrieval of cloud droplet size distribution from polarized observations of the cloudbow, *Atmospheric Measurement Techniques*, 16, 645–667, <https://doi.org/10.5194/amt-16-645-2023>, 2023.
- Remer, L. A., Knobelspiesse, K., Zhai, P.-W., Xu, F., Kalashnikova, O. V., Chowdhary, J., Hasekamp, O., Dubovik, O., Wu, L., Ahmad, Z., Boss, E., Cairns, B., Coddington, O., Davis, A. B., Dierssen, H. M., Diner, D. J., Franz, B., Frouin, R., Gao, B.-C., Ibrahim, A., Levy, R. C., Martins, J. V., Omar, A. H., and Torres, O.: Retrieving Aerosol Characteristics From the PACE Mission, Part 2: Multi-Angle and Polarimetry, *Frontiers in Environmental Science*, 7, <https://doi.org/10.3389/fenvs.2019.00094>, 2019.
- 720 R. C., Martins, J. V., Omar, A. H., and Torres, O.: Retrieving Aerosol Characteristics From the PACE Mission, Part 2: Multi-Angle and Polarimetry, *Frontiers in Environmental Science*, 7, <https://doi.org/10.3389/fenvs.2019.00094>, 2019.
- Stap, F., Hasekamp, O., Emde, C., and Röckmann, T.: Influence of 3D effects on 1D aerosol retrievals in synthetic, partially clouded scenes, *J. Quant. Spectrosc. Radiat. Transfer*, 170, 54 – 68, <https://doi.org/http://dx.doi.org/10.1016/j.jqsrt.2015.10.008>, 2016a.
- Stap, F. A., Hasekamp, O. P., Emde, C., and Rockmann, T.: Multiangle photopolarimetric aerosol retrievals in the vicinity of clouds: Synthetic study based on a large eddy simulation, *J. Geophys. Res.*, 121, 12914–12935, <https://doi.org/10.1002/2016JD024787>, 2016b.
- 725 Sterzik, M. F., Bagnulo, S., Emde, C., and Manev, M.: The cloudbow of planet Earth observed in polarisation, *Astron. Astrophys.*, 639, A89, <https://doi.org/10.1051/0004-6361/202038270>, 2020.
- Stevens, B., Bony, S., Farrell, D., Ament, F., Blyth, A., Fairall, C., Karstensen, J., Quinn, P. K., Speich, S., Acquistapace, C., Aemisegger, F., Albright, A. L., Bellenger, H., Bodenschatz, E., Caesar, K.-A., Chewitt-Lucas, R., de Boer, G., Delanoë, J., Denby, L., Ewald, F., Fildier, B., Forde, M., George, G., Gross, S., Hagen, M., Hausold, A., Heywood, K. J., Hirsch, L., Jacob, M., Jansen, F., Kinne, S., Klocke, D., Kölling, T., Konow, H., Lathon, M., Mohr, W., Naumann, A. K., Nuijens, L., Olivier, L., Pincus, R., Pöhlker, M., Reverdin, G., Roberts, G., Schnitt, S., Schulz, H., Siebesma, A. P., Stephan, C. C., Sullivan, P., Touzé-Peiffer, L., Vial, J., Vogel, R., Zuidema, P., Alexander, N., Alves, L., Arixi, S., Asmath, H., Bagheri, G., Baier, K., Bailey, A., Baranowski, D., Baron, A., Barrau, S., Barrett, P. A., Batier, F., Behrendt, A., Bendinger, A., Beucher, F., Bigorre, S., Blades, E., Blossey, P., Bock, O., Böing, S., Bossler, P., Bourras, D., Bouruet-Aubertot, P., Bower, K., Branellec, P., Branger, H., Brennek, M., Brewer, A., Brilouet, P.-E., Brüggmann, B., Buehler, S. A., Burke, E., Burton, R., Calmer, R., Canonici, J.-C., Carton, X., Cato Jr., G., Charles, J. A., Chazette, P., Chen, Y., Chilinski, M. T., Choulaton, T., Chuang, P., Clarke, S., Coe, H., Cornet, C., Coutris, P., Couvreux, F., Crewell, S., Cronin, T., Cui, Z., Cuypers, Y., Daley, A., Damerell, G. M., Dauhut, T., Deneke, H., Desbios, J.-P., Dörner, S., Donner, S., Douet, V., Drushka, K., Dütsch, M., Ehrlich, A., Emanuel, K., Emmanouilidis, A., Etienne, J.-C., Etienne-Leblanc, S., Faure, G., Feingold, G., Ferrero, L., Fix, A., Flamant, C., Flatau, P. J., Foltz, G. R., Forster, L., Furtuna, I., Gadian, A., Galewsky, J., Gallagher, M., Gallimore, P., Gaston, C., Gentemann, C., Geyskens, N., Giez, A., Gollop, J., Gouirand, I., Gourbeyre, C., de Graaf, D., de Groot, G. E., Grosz, R., Güttler, J., Gutleben, M., Hall, K., Harris, G., Helfer, K. C., Henze, D., Herbert, C., Holanda, B., Ibanez-Landeta, A., Intrieri, J., Iyer, S., Julien, F., Kalesse, H., Kazil, J., Kellman, A., Kidane, A. T., Kirchner, U., Klingebiel, M., Körner, M., Kremper, L. A., Kretzschmar, J., Krüger, O., Kumala, W., Kurz, A., L'Hégaret, P., Labaste, M., Lachlan-Cope, T., Laing, A., Landschützer, P., Lang, T., Lange, D., Lange, I., Laplace, C., Lavik, G., Laxenaire, R., Le Bihan, C., Leandro, M., Lefevre, N., Lena, M., Lenschow, D., Li, Q., Lloyd, G., Los, S., Losi, N., Lovell, O., Luneau, C., Makuch, P., Malinowski, S., Manta, G., Marinou, E., Marsden, N., Masson, S., Maury, N., Mayer, B., Mayers-Als, M., Mazel, C., McGeary, W., McWilliams, J. C., Mech, M., Mehlmann, M., Meroni, A. N., Mieslinger, T., Minikin, A., Minnett, P., Möller, G., Morfa Avalos, Y., Muller, C., Musat, I., Napoli, A., Neuberger, A., Noisel, C., Noone, D., Nordsiek, F., Nowak, J. L., Oswald, L., Parker, D. J., Peck, C., Person, R., Philippi, M., Plueddemann, A., Pöhlker, C., Pörtge, V., Pöschl, U., Pologne, L., Posyniak, M., Prange, M., Quiñones Meléndez, E., Radtke, J., Ramage,
- 730
735
740
745

- 750 K., Reimann, J., Renault, L., Reus, K., Reyes, A., Ribbe, J., Ringel, M., Ritschel, M., Rocha, C. B., Rochetin, N., Röttenbacher, J., Rollo, C., Royer, H., Sadoulet, P., Saffin, L., Sandiford, S., Sandu, I., Schäfer, M., Schemann, V., Schirmacher, I., Schlenczek, O., Schmidt, J., Schröder, M., Schwarzenboeck, A., Sealy, A., Senff, C. J., Serikov, I., Shohan, S., Siddle, E., Smirnov, A., Späth, F., Spooner, B., Stolla, M. K., Szkółka, W., de Szoeko, S. P., Tarot, S., Tetoni, E., Thompson, E., Thomson, J., Tomassini, L., Totems, J., Ubele, A. A., Villiger, L., von Arx, J., Wagner, T., Walther, A., Webber, B., Wendisch, M., Whitehall, S., Wiltshire, A., Wing, A. A., Wirth, M., Wiskandt, J.,
- 755 Wolf, K., Worbes, L., Wright, E., Wulfmeyer, V., Young, S., Zhang, C., Zhang, D., Ziemer, F., Zinner, T., and Zöger, M.: EUREC⁴A, Earth System Science Data, 13, 4067–4119, <https://doi.org/10.5194/essd-13-4067-2021>, 2021.
- Stubenrauch, C. J., Kinne, S., Mandorli, G., Rossow, W. B., Winker, D. M., Ackerman, S. A., Chepfer, H., Di Girolamo, L., Garnier, A., Heidinger, A., Karlsson, K.-G., Meyer, K., Minnis, P., Platnick, S., Stengel, M., Sun-Mack, S., Veglio, P., Walther, A., Cai, X., Young, A. H., and Zhao, G.: Lessons Learned from the Updated GEWEX Cloud Assessment Database, Surveys in Geophysics, <https://doi.org/10.1007/s10712-024-09824-0>, 2024.
- 760 Tsang, L., Kong, J. A., and Shin, R. T.: Theory of Microwave Remote Sensing, John Wiley, New York, 1985.
- Van Dienenhoven, B., Hasekamp, O. P., and Landgraf, J.: Retrieval of cloud parameters from satellite-based reflectance measurements in the ultraviolet and the oxygen A-band, Journal of Geophysical Research: Atmospheres, 112, 2006JD008155, <https://doi.org/10.1029/2006JD008155>, 2007.
- 765 Volkmer, L., Pörtge, V., Jakub, F., and Mayer, B.: Model-based evaluation of cloud geometry and droplet size retrievals from 2-D polarized measurements of specMACS, EGU sphere, 2023, 1–22, <https://doi.org/10.5194/egusphere-2023-2235>, 2023.
- Weber, A., Kölling, T., Pörtge, V., Baumgartner, A., Rammeloo, C., Zinner, T., and Mayer, B.: Polarization upgrade of specMACS: calibration and characterization of the 2D RGB polarization resolving cameras, EGU sphere, pp. 1–29, <https://doi.org/10.5194/egusphere-2023-2209>, 2023.
- 770 Wentz, F. J., Hilburn, K., and Smith, D. K.: RSS SSMIS OCEAN PRODUCT GRIDS DAILY FROM DMSP F17 NETCDF V7, Dataset available online from the NASA Global Hydrometeorology Resource Center DAAC, Huntsville, Alabama, U.S.A., <https://doi.org/http://dx.doi.org/10.5067/MEASURES/DMSP-F17/SSMIS/DATA301>, 2012.
- Wielicki, B. A. and Parker, L.: On the determination of cloud cover from satellite sensors: The effect of sensor spatial resolution, Journal of Geophysical Research: Atmospheres, 97, 12 799–12 823, <https://doi.org/https://doi.org/10.1029/92JD01061>, 1992.
- 775 Wiscombe, W.: Improved Mie scattering algorithms, Appl. Opt., 19, 1505–1509, 1980.
- Yu, H., Emde, C., Kylling, A., Veihelmann, B., Mayer, B., Stebel, K., and Van Roozendael, M.: Impact of 3D cloud structures on the atmospheric trace gas products from UV–Vis sounders – Part 2: Impact on NO₂ retrieval and mitigation strategies, Atmospheric Measurement Techniques, 15, 5743–5768, <https://doi.org/10.5194/amt-15-5743-2022>, 2022.
- Zhan, Y., Yi, F., Liu, F., Zhang, Y., Yu, C., and Zhou, J.: Convective Boundary Layer Clouds as Observed with Ground-Based Lidar at a
- 780 Mid-Latitude Plain Site, Remote Sensing, 13, <https://doi.org/10.3390/rs13071281>, 2021.
- Zinner, T., Wind, G., Platnick, S., and Ackerman, A. S.: Testing remote sensing on artificial observations: impact of drizzle and 3-D cloud structure on effective radius retrievals, Atmos. Chem. Phys., 10, 9535–9549, 2010.